

Universal activated aging and weak ergodicity breaking in spin and structural glasses

Bin Li,^{1, 2,*} Deng Pan,^{1,*} Ting Qu,^{1, 2} and Yuliang Jin^{1, 2, 3, †}

¹*Institute of Theoretical Physics, Chinese Academy of Sciences, Beijing 100190, China*

²*School of Physical Sciences, University of Chinese Academy of Sciences, Beijing 100049, China*

³*Center for Theoretical Interdisciplinary Sciences, Wenzhou Institute,*

University of Chinese Academy of Sciences, Wenzhou, Zhejiang 325001, China

(Dated: January 13, 2026)

Glasses possess complex energy landscapes and exhibit non-equilibrium aging dynamics. Here, we propose a generalized trap model for activated aging based on a key static property of the energy landscape: the distribution of energy barriers. Our theory predicts that, upon cooling, weak ergodicity breaking (WEB) in quenching dynamics occurs prior to strong ergodicity breaking in equilibrium dynamics. Furthermore, the theory indicates that the characteristic size of activation clusters can be deduced from the logarithmic decay of the time-correlation function. We rigorously test the model's assumptions and predictions using the simplest spin glass model - the random energy model. The predicted aging behavior is also universally observed in paradigmatic structural glasses, including the Weeks-Chandler-Andersen (WCA) model and amorphous silica. Remarkably, applying our framework to the WCA model allows us to extract a static length from the non-equilibrium dynamics, extending its observable growth range from a mere factor of 2-3 to a full order of magnitude and providing supportive evidence for the random first-order transition scenario. Finally, we propose a unified ergodic-WEB phase diagram for aging dynamics in general glassy systems.

Teaser: Weak ergodicity breaking occurs prior to strong ergodicity breaking in spin and structural glasses.

INTRODUCTION

Glassy systems, including spin glasses [1], structural glasses [2], polymers [3], colloidal suspensions [4], granular materials [5], active matter [6] and artificial neural networks [7], are characterized by multiple thermodynamically metastable states (glass basins) that are separated by energy barriers in the energy landscape [8], and non-equilibrium aging dynamics [9–11]. Aging refers to the dynamical slowing down of relaxation processes with an increasing “age” quantified by the waiting time (or the aging time) t_w elapsed after the system is quenched. Understanding aging represents a major theoretical challenge. Three approaches have been developed.

(i) *Mean-field theories.* In mean-field glass models, aging is described by a set of closed equations for the two-time correlation and response functions [12–18]. Mean-field aging corresponds to slow descent in the (free) energy landscape after quenching, during which paths to find lower energies become more and more scarce – called an “entropic effect” [9, 19–21]. Because energy barriers are infinite in mean-field models (in the thermodynamic limit), activated barrier-crossing processes do not occur in mean-field aging. Efforts to go beyond the mean-field approximation proceed mainly in the following two directions.

(ii) *Phenomenological trap models: random walk in a complex energy landscape.* Trap models [22, 23] are based on an intuitive picture that the evolution of a glass system can be described by the dynamics of a random walker in a complex multidimensional energy landscape [24, 25]. The random walker is typically “trapped” in a metastable glass basin (trap), within a trapping time τ , whose distribution is determined by the property of the landscape. With an increasing t_w , the probability of the system being trapped in deeper basins increases, which results in a longer hopping time to escape the basin and thus slower relaxation dynamics.

(iii) *Coarsening mechanism in real space.* The aging effects have also been analyzed during coarsening processes in the paradigmatic Ising model [26], models with quenched interaction disorder or random field [27, 28], and kinetically constrained models with facilitated dynamics [29]. Aging is generally characterized by logarithmic growth of the domain size.

To understand aging in real glassy systems, it is inevitable to go beyond mean-field approximations. The landscape-based approach, which we follow in the current study, is particularly attractive due to its simplicity and deep connections to general stochastic processes modeled by continuous-time random walk [30, 31]. The trap model is initially proposed by Bouchaud (BTM) [22, 23] to describe aging dynamics in the simplest spin glass model [32], i.e., the random energy model (REM) [33]. An inspiring outcome from the BTM is the so-called weak ergodicity breaking (WEB) in the spin glass phase, where the non-equilibrium correlation function converges, in the large-time limit, to a plateau whose value is determined by the so-called arcsin law [23]. Such asymptotic solutions of the BTM are supported by recent rigorous mathematical derivations [34–37]. However, this result is

* These two authors contributed equally

† yuliangjin@mail.itp.ac.cn

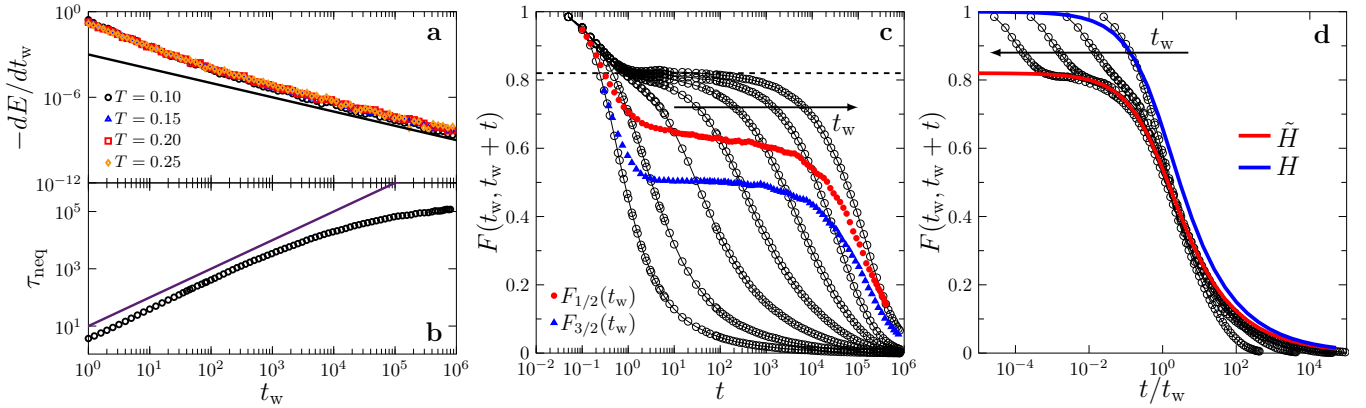


FIG. 1. Basic aging phenomenon in glasses. Data are obtained for the WCA model at $T = 0.25$ with $N = 8000$ particles, quenched from $T_{\text{eq}} = 5$ to T . (a) $-dE/dt_w$ as a function of t_w at a few different T . The solid line indicates $-dE/dt_w \sim t_w^{-1}$, i.e., $E(t_w) \sim -\ln(t_w)$. (b) Non-equilibrium decorrelation time τ_{neq} as a function of t_w . The solid line represents $\tau_{\text{neq}} \sim t_w$. (c) $F(t_w, t_w + t)$ for $t_w = 0.2, 2, 20, 2 \times 10^2, 2 \times 10^3, 2 \times 10^4, 8 \times 10^5$ (black curves; from left to right), and $F_w(t_w)$ with $w = 1/2$ and $w = 3/2$. The dashed line indicates the nonergodicity parameter f . (c) $F(t_w, t_w + t)$ plotted as a function of $w = t/t_w$ for intermediate waiting times $t_w = 2, 20, 2 \times 10^2, 2 \times 10^3$. The blue line is H given by Eq. (2) at the given $\hat{x} = T/T_{\text{WEB}}$, and the red line is $\tilde{H} = fH$.

inconsistent with Monte Carlo (MC) simulations of the REM (with Gaussian random energies) consisting of a finite number N of spins [38, 39]: the obtained aging functions do not show any sign of convergence to the predicted plateau. Obviously, before any rigorous extension can be made, a fundamental task is to reconcile the inconsistency between the theory and MC simulations in the REM. Once this mission is accomplished, the next natural question is about the relevance of trap model predictions to the aging behavior in more realistic glasses [40]. Both problems are addressed in the present study.

Here we propose a generalized trap model (GTM), which takes into account the finite-size corrections in the barrier energy distribution. The GTM theory predicts that the WEB in non-equilibrium aging occurs at a temperature T_{WEB} , above the strong (standard) ergodicity breaking (SEB) temperature T_{SEB} in equilibrium dynamics. This WEB corresponds to the point where the large-waiting-time limit and large-system-size limit (thermodynamic limit) become non-interchangeable. The theory also explains that the logarithmic decay in the time-correlation aging function is associated with the finite spatial size of activated events. The GTM predictions are consistent with simulation results of four models: random energy spin glass models with Gaussian and exponential energy distributions, Weeks-Chandler-Andersen (WCA) structural glass model, and amorphous silica (SiO_2) network glass model. Remarkably, combining the theoretical formalism and simulation data, a static length ξ_{ag} characterizing the size of activation patches can be extracted from non-equilibrium aging dynamics in the WCA model. The ξ_{ag} data, although lying in a much lower temperature regime, are on the same curve of other static lengths,

including the point-to-set (PTS) length ξ_{PTS} [41, 42] and the static length ξ_{Hessian} obtained from vibrational properties [43]. Combining the three lengths together, the growth range of the static length is extended from a factor of $2 \sim 3$ existing in the literature to one decade, showing supporting evidence of the random first order transition (RFOT) prediction $\xi \sim (T - T_K)^{-\nu}$ with a finite Kauzmann temperature T_K and $\nu \approx 0.61$ [44, 45]. Our results are summarized by a phase diagram that can universally describe ergodic and WEB phases in spin and structural glasses.

RESULTS

Basic aging phenomenon and weak ergodicity breaking

The aging phenomenon in glasses is typically studied as follows. Starting from an equilibrium configuration at a high temperature T_{eq} , one rapidly quenches the system to a final temperature $T < T_{\text{eq}}$, and lets the system evolve at a constant temperature T (the time is set to zero $t = 0$ after quenching). The system is out of equilibrium after quenching, and the following relaxation dynamics are accompanied by aging effects.

The aging dynamics can be monitored by one-time observables, such as the potential energy $E(t_w)$, which typically shows slow decay close to a logarithmic time-dependent function, $E(t_w) \sim -\ln(t_w)$ (see Fig. 1a; to be explicit, in Fig. 1 we focus on the simulation results of the WCA model). More informative descriptors are two-time correlation functions, $C(t_w, t_w + t) = \langle A^*(t_w)A(t_w + t) \rangle$, where A is a physical observable, t_w the waiting time

elapsed after quenching, and $\langle \dots \rangle$ the average over initial configurations. In structural glasses, one typically takes $A(t) = e^{i\mathbf{q} \cdot \mathbf{r}_i(t)}$, where $\mathbf{r}_i(t)$ is the position of particle i at time t , and \mathbf{q} is a wave-vector - then $F_q(t_w, t_w + t) = \frac{1}{N} \langle \sum_{i=1}^N e^{i\mathbf{q} \cdot [\mathbf{r}_i(t_w + t) - \mathbf{r}_i(t_w)]} \rangle$ is essentially the non-equilibrium generalization of the standard incoherent scattering function. In spin glasses, it is natural to consider the spin-spin correlations, $C(t_w, t_w + t) = \frac{1}{N} \langle \sum_{i=1}^N S_i(t_w) S_i(t_w + t) \rangle$. Here N represents the system size, i.e., number of particles or spins. Figure 1b shows that $F_q(t_w, t_w + t)$ in the WCA model has a strong dependence on t_w , which is direct evidence of non-equilibrium dynamics. Following the convention, in this study we focus on a fixed $q = q_{\max}$, where q_{\max} is the location of the maximum in the structural factor $S(q)$. The subscript of q in F_q will be omitted from now on.

It can be argued that, in many cases, the key object describing aging is the reduced one-time correlation function (*aging function*), $C_w(t_w) \equiv C[t_w, (1+w)t_w]$ with the ratio $t/t_w = w$ fixed. This is based on the following considerations. First, aging effects are only observable after a time scale in the order of t_w - at short times, the correlation functions $F(t_w, t_w + t)$ is t_w -independent (see Fig. 1c) [46]. Second, if plotted as a function of t/t_w , $F(t_w, t_w + t)$ satisfies $F(t_w, t_w + t) = F^{\text{st}}(t) + F^{\text{ag}}(t/t_w)$ for intermediate t_w (see Fig. 1d). Here the first term $F^{\text{st}}(t)$ corresponds to short-time microscopic dynamics that are t_w -independent. The collapsed term $F^{\text{ag}}(t/t_w)$ is the aging part that we aim to understand. Note that curves with very small t_w and very large t_w , corresponding to microscopic and equilibrium dynamics respectively, do not collapse. The non-equilibrium decorrelation time, defined by $F(t_w, t_w + \tau_{\text{neq}}) = 1/e$, is nearly proportional to t_w in the aging regime, $\tau_{\text{neq}}(t_w) \sim t_w$ (see Fig. 1b). At large times, $\tau_{\text{neq}}(t_w)$ reaches a plateau, $\tau_{\text{neq}}(t_w \rightarrow \infty) = \tau_{\text{eq}}$, due to thermalization. Although a more general rescaling form has been proposed based on the coarsening mechanism, $C(t_w, t_w + t) = C^{\text{st}}(t) + C^{\text{ag}}[h(t + t_w)/h(t_w)]$ [26], here we will only consider the simplistic case, $h(t) \sim t$, which already captures well the simulation results. Third, $C_w(t_w)$ can be theoretically analyzed by trap models, with asymptotic behavior given by the arcsin law [9, 22, 23].

A remarkable property associated with $C_w(t_w)$ is the WEB behavior, originally noticed by Bouchaud in the analysis of the BTM [12, 18, 22, 23]. One is interested in the following question: if the system is quenched from T_{eq} to a low temperature T and waited for a time t_w , can it relax after a time $t = w t_w$? Mathematically, the WEB is defined by the condition when $C_w(t_w)$ does not decay to zero in the large- t_w limit: $C_w(t_w \rightarrow \infty) > 0$ for $T < T_{\text{WEB}}$, and $C_w(t_w \rightarrow \infty) = 0$ for $T > T_{\text{WEB}}$, where T_{WEB} is the WEB temperature. Such WEB is observable in the simulated $F_w(t_w) \equiv F[t_w, (1+w)t_w]$ with a fixed w at $T = 0.25$ (see Fig. 1c). The plateau in the intermediate time ($10^0 < t_w < 10^4$) is evidence of WEB. The decay from this plateau at large t_w is due to thermalization, which is not considered by the current

theoretical model.

Intuitively, the WEB indicates the detection of the energy landscape in non-equilibrium aging dynamics when $T < T_{\text{WEB}}$. The system “feels” the energy landscape only when the time scales of fast and activated dynamics are separable. In this case, according to the Arrhenius law, the system is typically trapped in a metastable glass basin with an energy barrier $\Delta E \sim k_B T \ln(t_w)$ after a waiting time t_w (we will neglect the Boltzmann constant $k_B = 1$ in the expressions below by setting it as the unit). The time required to escape this basin is $\tau \sim e^{\Delta E/T} \sim t_w$. In other words, whenever the system feels the landscape, ergodicity breaks down within the timescale $t \sim t_w$. However, such ergodicity breaking is “weak” in the sense that the system relaxes after a time scale t much larger than t_w . Indeed, for a finite, fixed t_w , $\lim_{t \rightarrow \infty} F(t_w, t_w + t) = 0$ at the same T . As shown by Fig. 1c, in the time regime $10^0 < t_w < 10^4$ where $F_w(t_w)$ exhibits a plateau, the two-time function $F(t_w, t_w + t)$ for a fixed t_w rapidly decays with an increasing t , showing no sign of a plateau.

The WEB in non-equilibrium aging dynamics is, by definition, different from the SEB. The SEB occurs at a temperature T_{SEB} where the phase space becomes disconnected. Mathematically, the SEB is described by the equilibrium time-correlation function, $C_{\text{eq}}(t) = \langle C_{\text{eq}}(t_0, t_0 + t) \rangle_{t_0}$, where $\langle \dots \rangle_{t_0}$ is the average over the reference time t_0 based on the time translation invariance: $C_{\text{eq}}(t \rightarrow \infty) > 0$ for $T < T_{\text{SEB}}$, and $C_{\text{eq}}(t \rightarrow \infty) = 0$ for $T > T_{\text{SEB}}$. In mean-field spin glass models, T_{SEB} corresponds to the well-defined thermodynamic spin glass transition temperature T_c , $T_{\text{SEB}} = T_c$. In finite-dimensional structural glasses, T_{SEB} corresponds to the mode-coupling theory (MCT) crossover temperature T_{MCT} , where the equilibrium relaxation time τ_{eq} is expected to diverge. The difference between WEB and SEB is clearly visible in Fig. 1c. The plateau (called a nonergodicity parameter f) associated with SEB appears in $F_{\text{eq}}(t)$, which is the envelope of $F(t_w, t_w + t)$ curves. This equilibrium plateau is not the same plateau in $F_w(t_w)$ - they have different physical meanings as explained above.

The main purpose of our theoretical modeling below is to explain the behavior of $C_w(t_w)$ and the difference between T_{WEB} and T_{SEB} . We will begin by reviewing the BTM model and discussing its inconsistency with simulation results.

Bouchaud’s trap model

In the BTM, the trapping time τ in a metastable glass basin is related to the energy barrier ΔE of that basin through the Arrhenius law, $\tau \sim \exp(\Delta E/T)$. The trajectory of the random walker consists of a sequence of hops in the energy landscape with a trapping time distribution $\psi(\tau)$ that is determined by the energy barrier distribu-

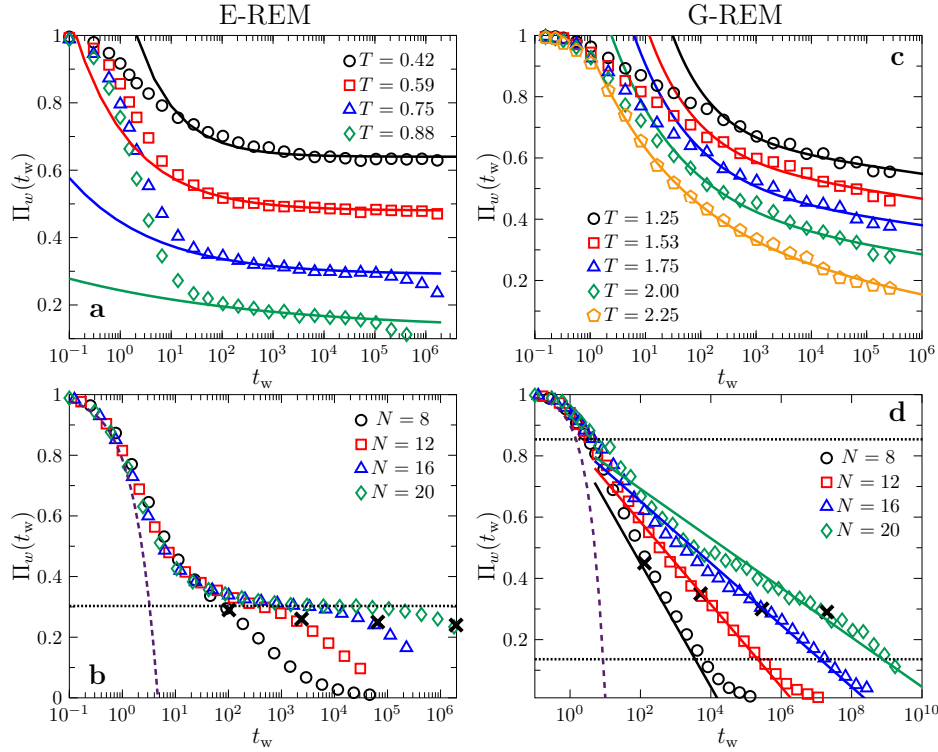


FIG. 2. Aging function $\Pi_w(t_w)$ for the (a,b) E-REM and (c-d) G-REM. In both models, $w = 0.5$. Open points are MC simulation data. (a) E-REM results with $N = 20$ (points). Data in the plateau regime are fitted by $\Pi(t_w) = H(1 + A t_w^{-\alpha})$ (lines). (b) E-REM data at $T = 0.75$. The purple dashed line represents the short-time behavior $\Pi_w^s(t_w) = 1 - Ct_w$ with $C \approx 0.214$. The dotted horizontal line represents the BTM plateau $H(w, x) \approx 0.303$. The thermalization time $\tau_{\text{th}} = \exp(N/T)$ is marked by crosses. (c) G-REM results with $N = 128$ (points). Data at large times are fitted by $\Pi(t_w) = H(1 + A t_w^{-\alpha}) - k \ln t_w$ (lines). (d) At $T = 0.75$, the G-REM data are dominated by logarithmic decay $\Pi(t_w) \sim -\frac{B}{N} \ln t_w$ (lines) in small systems, where $B = 0.7$ is a fitting parameter. The horizontal dashed lines represent the GTM plateau $H(w, \hat{x}) \approx 0.854$ and the BTM plateau $H(w, x) \approx 0.136$. The fitting parameters H and α for both models are plotted in Fig. 7(a,b).

tion $P(\Delta E)$. A further assumption is that consecutive hops are uncorrelated (called *renewal mechanism*), i.e., $\psi(\tau_1, \tau_2) = \psi(\tau_1)\psi(\tau_2)$.

The key input to the BTM is the energy barrier distribution $P(\Delta E)$ - once $P(\Delta E)$ is given, in principle the dynamics of the system can be reconstructed, with the setup described above. For example, one can compute $\Pi(t_w, t_w + t)$ that describes the probability of not leaving the glass basin between two times t_w and $t_w + t$ after quenching, which is related to the spin auto-correlation function via $C^{\text{ag}}(t_w, t_w + t) = q_{\text{EA}}\Pi(t_w, t_w + t)$, with q_{EA} the Edwards-Anderson order parameter [20]. The BTM assumes an exponential distribution [22, 23],

$$p_{\text{BTM}}(\Delta E) \sim \exp(-\Delta E/T_c). \quad (1)$$

In the REM, it was claimed that T_c corresponds to the spin glass transition temperature (see Materials and Methods A for the details of the REM). The exponential form Eq. (1) is consistent with mean-field thermodynamic calculations for the glass models in the so-called the one-step replica symmetry breaking (1-RSB) universality class [1]. Interestingly, Eq. (1) is formally identical to the Boltzmann distribution, $P(E) \sim \exp(-E/T)$,

of the microstate energy in an equilibrium system - the only difference is the replacement of T by a constant T_c . Because $P(\Delta E)$ is a static property of the energy landscape, it should be T -independent; then a natural guess of the parameter T_c in Eq. (1) is the glass transition temperature, which is the only characteristic temperature in simple models such as the REM.

According to Eq. (1) and the Arrhenius law, τ follows a power-law distribution, $\psi(\tau) \sim \tau^{-(1+x)}$, where $x = T/T_c$ is the reduced temperature. Because $0 < x < 1$ below T_c , the average trapping time $\langle \tau \rangle$ diverges in the glass phase. Thus the system takes infinite time to reach equilibrium, leading to long-time aging and WEB. Mathematically, WEB is described by the arcsin law [47]:

$$\lim_{t_w \rightarrow \infty} \Pi_w(t_w) = \frac{\sin(\pi x)}{\pi} \int_w^\infty \frac{du}{u^x(1+u)} \equiv H(w, x). \quad (2)$$

Here $H(w, x)$ is a *weak ergodicity breaking order parameter*: $H(w, x) = 0$ in the ergodic phase, and $H(w, x) > 0$ in the WEB phase. Importantly, the BTM predicts that the WEB and spin glass transition occurs simultaneously, $T_{\text{WEB}} = T_c$. We will show below that this prediction is inconsistent with simulation results.

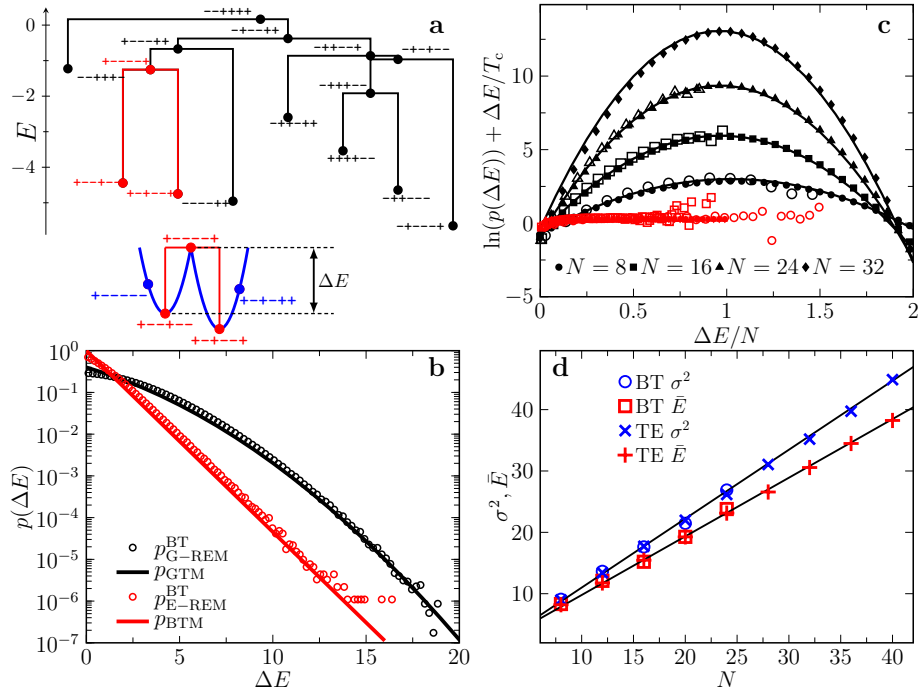


FIG. 3. Barrier energy distributions in the G-REM and E-REM. (a) A sub-tree formed by local minima and saddle points for the $N = 6$ G-REM obtained by the BT algorithm, with corresponding spin configurations and energies (E -axis) indicated. (inset) Illustration of two traps: the blue nodes are non-minimum-non-saddle configurations; the barrier energy ΔE is the energy difference between the local minimum and saddle point. (b) Distributions $p_{G-REM}^{BT}(\Delta E)$ and $p_{E-REM}^{BT}(\Delta E)$ of the G-REM and E-REM by the BT algorithm ($N = 20$), compared to $p_{BTM}(\Delta E)$ (Eq. 1) and $p_{GTM}(\Delta E)$ (Eq. 3 with $a = 1.12$ and $b = 0.96$). (c) Remainder $\ln(p(\Delta E) + \Delta E/T_c)$ for the G-REM (black) and E-REM (red). Open and filled points are obtained by the BT algorithm and TE theory respectively. Lines represent fitting to a Gaussian function. The variance σ^2 and mean \bar{E} obtained by the Gaussian fitting are plotted in (d) as functions of N . Linear fitting of the data in (d) gives $a = 1.12$ and $b = 0.96$ ($\sigma^2 = aN$ and $\bar{E} = bN$).

With the given theoretical assumptions, the arcsin law Eq. (2) is proven to be rigorous in the thermodynamic and large-time limits (taking $N \rightarrow \infty$ first and then $t_w \rightarrow \infty$) [35, 48]. It was expected that such rigorous results would apply to the REM. However, the arcsin law is challenged by the single-spin flip MC simulations of the standard REM with a Gaussian distribution of configuration energy (G-REM), as shown in [38]. Up to the largest system size and time ($N \sim 20$ and $t_w \sim 10^{10}$) that can be simulated by regular CPUs, there is no sign that the simulation data of $\Pi_w(t_w)$ would converge to the predicted plateau $H(w, x)$ (see also Fig. 2d). In contrast, such convergence is well observed in the REM with an exponential distribution of energy (E-REM) [38] (see also Fig. 2b). Thus the aging theory built on the phenomenological BTM cannot fully explain the asymptotic dynamics in simple models such as the REM.

Generalized trap model

To understand why the BTM fails to describe the simulation results, one should naturally re-examine the underlying assumptions. Based on the numerical data obtained

for REMs, we have examined three major assumptions as described above: (i) the Arrhenius law $\tau \sim \exp(\Delta E/T)$, (ii) the renewal mechanism $\psi(\tau_1, \tau_2) = \psi(\tau_1)\psi(\tau_2)$, and (iii) the exponential barrier distribution Eq. (1). We find that the first two assumptions hold, but the third one requires correction (see below). Based on these observations, we propose a GTM, which retains all assumptions of the original BTM, except for the exponential barrier distribution. In the GTM, we add a Gaussian correction term to the barrier distribution,

$$p_{GTM}(\Delta E) \sim \exp \left[-\frac{\Delta E}{T_c} - \frac{(\Delta E - \bar{E})^2}{2Na} \right], \quad (3)$$

where a is a model-dependent parameter. The energy scale $\bar{E} = bN$ is assumed to be extensive, where b is also model-dependent. Note that the Gaussian term, which follows the standard central limit theorem, is essentially caused by finite-size effects. Equation (3) will be explicitly examined in the REMs below, but for now, we take it as input and derive the corresponding aging function theoretically (see details in the Supplementary Materials, SM, Sec. S1).

There are two crucial dynamical consequences due to the Gaussian term in Eq. (3). The first consequence is the

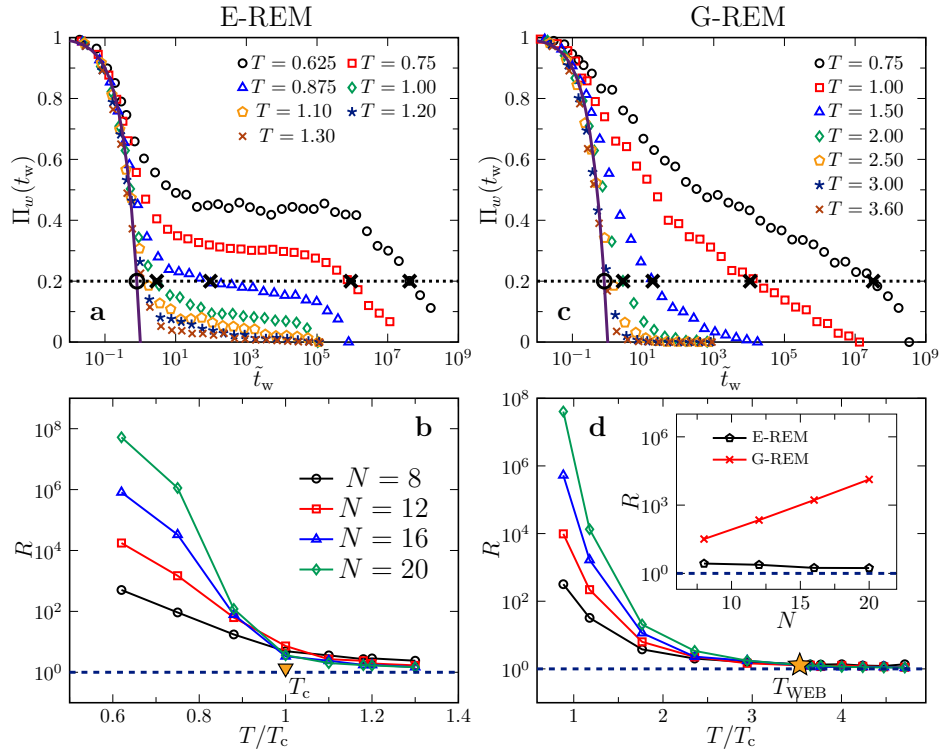


FIG. 4. WEB in (a,b) E-REM and (c,d) G-REM. In (a,c), $\Pi_w(t_w)$ is obtained with $N = 20$ and $w = 0.5$ by MC simulations at the rescaled time $\tilde{t}_w = C t_w$ with $C = \frac{w\hat{x}}{1+\hat{x}}$. The solid line is $\Pi_w^0(\tilde{t}_w) = 1 - \tilde{t}_w$ (see Eq. 5). The dotted horizontal line is $\Pi_{\text{thr}} = 0.2$. The time scales $\tilde{\tau}^0$ (circle) and $\tilde{\tau}$ (cross) are marked. (b,d) $R = \tilde{\tau}/\tilde{\tau}^0$ as a function of T for different N . (inset) R as a function of N at $T = 1.17 T_c$.

modification of the asymptotic plateau $H(w, x)$ in Eq. (2) with $x = T/T_c$ replaced by an effective $\hat{x} = T/T_{\text{WEB}}$. The second consequence introduces a logarithmic decay term $\sim \frac{1}{N} \ln t_w$ in the pre-asymptotic behavior of $\Pi_w(t_w)$, which avoids the asymptotic plateau in small systems. Next we discuss them in detail.

Expanding Eq. (3) gives (neglecting the constant term), $\ln p_{\text{GTM}}(\Delta E) \sim -\frac{1}{T_c} \left(1 - \frac{\bar{E} T_c}{N a} \right) \Delta E - \frac{1}{2 N a} \Delta E^2$. The linear coefficient suggests an effective x parameter, $\hat{x} = (1 - b T_c/a) x = (1 - W) T/T_c$, where the parameter $W = b T_c/a$ weights the contributions of linear and Gaussian terms in Eq. (3). Importantly, W is independent of N , and thus this modification does not disappear even in the thermodynamic limit. However, if we take $N \rightarrow \infty$ first in Eq. (3), then obviously the GTM degenerates with the BTM. It suggests that the double limits $N \rightarrow \infty$ and $t_w \rightarrow \infty$ are not interchangeable, once WEB occurs. In the rigorous analyses performed previously [34–37], the order is $N \rightarrow \infty$ first and then $t_w \rightarrow \infty$. However, in MC simulations, generally long-time simulations ($t_w \rightarrow \infty$) are performed for small N , then finite-size analysis is performed to extrapolate the behavior in the thermodynamic limit. In the latter case, the correction due to the Gaussian term is non-negligible even in large systems, which explains the discrepancy between simulation and rigorous results.

The asymptotic plateau of $H(w, x)$ still obeys the arcsin law Eq. (2), if x is replaced by \hat{x} . Interestingly, $H(w, \hat{x})$ suggests that the WEB occurs at,

$$T_{\text{WEB}} = \frac{T_c}{1 - W}, \quad (4)$$

which is above the glass transition temperature T_c . The ratio $T_{\text{WEB}}/T_c = 1/(1 - W)$ depends on the model, since W is model-dependent, as explained above.

The second interesting consequence is caused by the quadratic term $\sim \Delta E^2/N$ in Eq (3), which is $O(1/N)$. This term adds a logarithmic decay term (higher-order corrections are neglected) to the pre-asymptotic behavior of $\Pi_w(t_w)$, as derived in SM Sec. S1:

$$\Pi_w^{\text{GTM}}(t_w) \sim \begin{cases} 1 - C t_w, & t_w < \tau_m, \\ H(1 + A t_w^{-\alpha}) - \frac{B}{N} \ln t_w, & \tau_m < t_w < \tau_{\text{th}}, \\ \text{thermalization}, & t_w > \tau_{\text{th}}. \end{cases} \quad (5)$$

Here $\tau_m \sim O(1)$ is a microscopic time scale, and the rapid decay when $t_w < \tau_m$ is due to microscopic dynamics, with $C = \frac{w\hat{x}}{1+\hat{x}}$. The thermalization time τ_{th} depends on the largest energy barrier ΔE_{max} through $\tau_{\text{th}} \sim \exp(\Delta E_{\text{max}}/T)$; in the REMs, $\Delta E_{\text{max}} \sim N$ and therefore $\tau_{\text{th}} \sim \exp(N/T)$ (see Fig. 2b,d). We do not

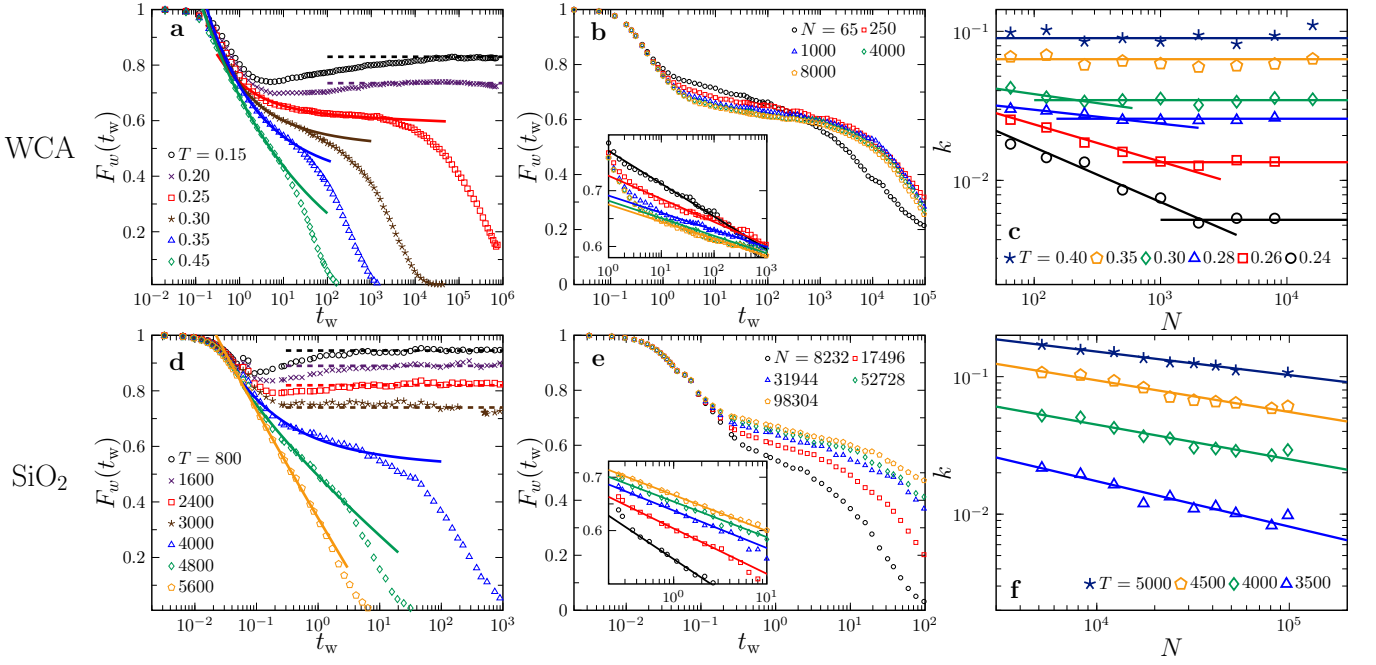


FIG. 5. Aging in (a-c) WCA and (d-f) amorphous silica models. (a) $F_w(t_w)$ obtained by MD simulations of the WCA model, with $N = 16000$. The data in the intermediate time regime are fitted to $F_w(t_w) = \tilde{H}(1 + A t_w^{-\alpha}) - k \ln t_w$ (solid lines). At the two lowest T , \tilde{H} is estimated by fitting the plateau (dashed lines), and α cannot be determined due to the presence of a dip. (b) $F_w(t_w)$ at $T = 0.26$ with different N . Inset is the close-up for the data in $1 < t_w < 10^3$, fitted to $F_w(t_w) \sim -k \ln t_w$ (lines). The parameter k obtained in this way is plotted in (c) as a function of N at different T . The crossover size n is determined by the intersect of two linear fitting lines (when $T < 0.35$). (d-e) Similar plots for amorphous silica (SiO₂). In (d,f), $N = 31944$; in (e), $T = 4000$ K. In all panels, $w = 1/2$. The parameters H and α are plotted in Fig. 7(a,b) for both models.

discuss the dynamics near and after τ_{th} in this study, although thermalization itself is a very interesting problem [49].

The most important part in Eq. (5) is the aging regime at intermediate times $\tau_m < t_w < \tau_{\text{th}}$. Expressions of the coefficients are obtained by theoretical calculations with the lowest-order approximation (see SM Sec. S1): $A = \frac{1}{(1-\hat{x})\Gamma(1-\hat{x})\Gamma^2(\hat{x})}$ with $\Gamma(x)$ a gamma function, and $B = \frac{T^2}{a} \frac{\partial H(w, \hat{x})}{\partial \hat{x}}$. The first term $H(1 + A t_w^{-\alpha})$ in Eq. (5) tells us that, in the limit $N \rightarrow \infty$, $\Pi_w(t_w)$ approaches the asymptotic limit $H(w, \hat{x})$ following a power-law function, with the exponent given by our theory:

$$\alpha = 1 - \frac{T}{T_{\text{WEB}}}. \quad (6)$$

The second term $-\frac{B}{N} \ln t_w$ implies that, when N is small, this logarithmic decay will destroy the asymptotic plateau - this is what we observe in simulations of G-REM.

It can be shown that the theoretical predictions from the GTM capture universal aging behavior in simulated spin and structural glasses: (i) with the model-dependent temperature T_{WEB} determined, the WEB order parameter H and the exponent α estimated from the simulation data collapse when plotted according to Eqs. (2) and (6); (ii) the logarithmic decay $-k \ln t_w$ in

$\Pi_w(t_w)$ can be universally observed at appropriate time and temperature windows in different models, and the coefficient k can be used to estimate the size of activation clusters. Below we demonstrate such universality with simulations of several spin and structural glass models.

Aging in spin glass random energy models

In REMs, we examine both the assumptions and predictions of the GTM. We first focus on the assumptions. As shown in SM Sec. S2, data obtained from numerical simulations are consistent with the Arrhenius law and renewal mechanism. Next we examine the barrier energy distribution, Eq. (3), using two independent approaches. The first one is an exhaustive enumeration of energy barriers using the barrier-tree (BT) algorithm [51–54] (see Fig. 3a for an example of a sub-tree and Materials and Methods A for algorithm details). The BT method provides the exact distribution $p^{\text{BT}}(\Delta E)$, but is restricted to small systems ($N \leq 20$). We also develop a tree-expansion (TE) theory to compute the distribution analytically and approximately, giving $p^{\text{TE}}(\Delta E)$ for any N (see SM Sec. S3). The difference between $p^{\text{BT}}(\Delta E)$ and $p^{\text{TE}}(\Delta E)$ is unnoticeable, as shown in Fig 3(b-d).

While the distribution $p_{\text{E-REM}}^{\text{BT}}(\Delta E)$ of the E-REM

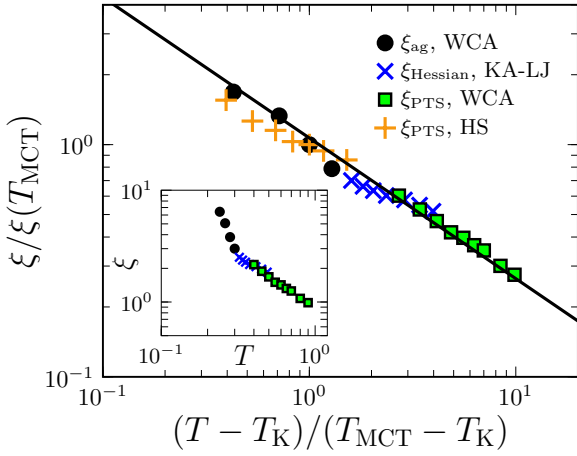


FIG. 6. Static lengths. The following data are plotted: ξ_{ag} for the WCA model (this work), ξ_{Hessian} for the KA-LJ model from [43] (T is rescaled by a factor of 3/4), ξ_{PTS} for the WCA model from [42], and ξ_{PTS} for HSSs from [50]. The HS ξ_{PTS} is plotted as a function of $(Z^{-1} - Z_{\text{K}}^{-1})/(Z_{\text{MCT}}^{-1} - Z_{\text{K}}^{-1})$. The black line represents the fitting $\xi \sim (T - T_{\text{K}})^{-\nu}$, where $T_{\text{K}} = 0.21$ and $\nu = 0.61(1)$. (inset) ξ as a function of T .

obtained by the BT algorithm is very close to the exponential form $p_{\text{BTM}}(\Delta E)$ (see Eq. 1), it is evident that the G-REM distribution $p_{\text{G-REM}}^{\text{BT}}(\Delta E)$ deviates from a pure exponential distribution (Fig. 3b). To analyze this deviation more carefully, the exponential part Eq. (1) is subtracted from the full distribution, and the remainder $\ln[p^{\text{BT}}(\Delta E)] + \Delta E/T_{\text{c}}$ is plotted in Fig. 3c for both models. The data for G-REM in Fig. 3c can be well fitted by a quadratic function $f(\Delta E) = c - \frac{(\Delta E - \bar{E})^2}{2\sigma^2}$. The variance $\sigma^2 = aN$ and mean $\bar{E} = bN$ linearly depend on N , as shown in Fig. 3d. From the linear fitting, we obtain $a = 1.12$ and $b = 0.96$ for the G-REM. In contrast, the remainder of the E-REM in Fig. 3c is negligible. Thus for the E-REM, the barrier distribution is well described by a pure exponential function as in the BTM.

Next we compare the GTM prediction Eq. (5) with the MC simulation data of REMs. For the E-REM, because the correction term in Eq. (3) is negligible, we can set $T_{\text{WEB}} = T_{\text{c}} = 1$ and expect $\Pi_w(t_{\text{w}}) \sim H(1 + A t_{\text{w}}^{-\alpha})$ in the aging regime. Fitting the data by this form, we obtain H and α for a few T with a fixed system size $N = 20$ (Fig. 2a). The fitted values of H and α are compared to the theoretical predictions Eq. (2) and (6) in Fig. 7(a,b), and good agreement is found. In Fig. 2b, we examine the finite-size effects, at a fixed $T = 0.75$. It can be seen that even for small systems $N = 8 - 20$, the BTM plateau can be well-observed. The analysis confirms that the logarithmic decay in Eq. (3) is not essential in E-REM, as expected.

For the G-REM, the Gaussian correction in Eq. (3) is non-negligible as shown in Fig. 3. Consequently, we need to use the full expression $\Pi_w(t_{\text{w}}) \sim H(1 + A t_{\text{w}}^{-\alpha}) - k \ln t_{\text{w}}$ to fit the data (see Fig. 2c). Here we have set $\hat{x} = T/T_{\text{WEB}}$, $T_{\text{WEB}} = T_{\text{c}}/(1 - W) \approx 3.6 T_{\text{c}}$ (see Eq. 4),

where $W = bT_{\text{c}}/a \approx 0.722$ with $a = 1.12$ and $b = 0.96$ from Fig. 3 and $T_{\text{c}} \approx 0.849$ from the literature [33]. The fitted H and α are compared to the theory in Fig. 7(a,b). The coefficient k depends on N as expected by the theory $k \sim 1/N$ (see Fig. 2d).

An interesting prediction from the GTM theory is that the WEB does not necessarily co-occur with the spin glass transition: for the E-REM, $T_{\text{WEB}} = T_{\text{c}}$, while for the G-REM, $T_{\text{WEB}} \approx 3.6 T_{\text{c}}$. The factor 3.6 in the G-REM is substantially larger than one - thus the GTM scenario ($T_{\text{WEB}} \approx 3.6 T_{\text{c}}$) can be unambiguously tested against the original BTM scenario ($T_{\text{WEB}} = T_{\text{c}}$) [22]. Below we directly verify the GTM scenario. In Fig. 4 we plot the MC data of $\Pi_w(t_{\text{w}})$ for both E-REM and G-REM, with t_{w} rescaled by $C = \frac{w\hat{x}}{1+\hat{x}}$ to collapse the short-time behavior $\Pi_w^0(t_{\text{w}}) = 1 - Ct_{\text{w}}$ at different T (note that C is not a fitting parameter). If WEB occurs, $\Pi_w(\tilde{t}_{\text{w}})$ should not vanish in the $\tilde{t}_{\text{w}} \rightarrow \infty$ limit, where $\tilde{t}_{\text{w}} \equiv Ct_{\text{w}}$ is the reduced waiting time. We define a time scale $\tilde{\tau}$ such that $\Pi_w(\tilde{t}_{\text{w}} = \tilde{\tau}) = \Pi_{\text{thr}}$ and choose a threshold $\Pi_{\text{thr}} = 0.2$. At sufficiently high T (in the ergodic phase), $\tilde{\tau} = \tilde{\tau}^0$ is a constant, where $\tilde{\tau}^0$ is defined by $\Pi_w^0(\tilde{t}_{\text{w}} = \tilde{\tau}^0) = 1 - \tilde{\tau}^0 = \Pi_{\text{thr}}$. As shown in Fig. 4, with an increasing T , the ratio $R = \tilde{\tau}/\tilde{\tau}^0$ approaches one around T_{c} in E-REM and around $T_{\text{WEB}} \approx 3.6 T_{\text{c}}$ in G-REM. According to the GTM scenario, we expect $R \rightarrow \infty$ below T_{WEB} in the thermodynamic limit, because $\tilde{\tau}$ should diverge in the WEB phase. This expectation is confirmed by finite-size analyses at a fixed $T = 1.17 T_{\text{c}}$ slightly above T_{c} in both models (see Fig. 4d-inset). In G-REM, R increases with N at this temperature; in contrast, in E-REM, $R \approx 1$ is nearly invariant. This is direct evidence of WEB above T_{c} in the G-REM.

Aging in structural glasses

To further examine the universality of the GTM theory, we simulate two structural glass formers: the WCA model as an example of simple molecular systems, and the amorphous silica (SiO_2) model as an example of network glasses (see Materials and Methods B and C for details). Because efficient sampling of energy barriers in structural glasses remains technically challenging [40, 61, 62], we will only compare the simulated aging function $\Pi_w(t_{\text{w}})$ to theoretical predictions (see the data in Fig. 5 with a fixed $w = 1/2$). Note that $\Pi_w(t_{\text{w}})$ is related to $F_w(t_{\text{w}})$ via $F_w(t_{\text{w}}) = f\Pi_w(t_{\text{w}})$, where f is the nonergodicity parameter defined by the large-time plateau value of the equilibrium incoherent scattering function $f = \lim_{t \rightarrow \infty} F_{\text{eq}}(t)$. The nonergodicity parameter f is analogous to the Edwards-Anderson order parameter q_{EA} in spin glasses, both of which are determined by the typical size of the glass basins.

We first extract H and α from the aging data, and compare them to theoretical predictions. As shown in

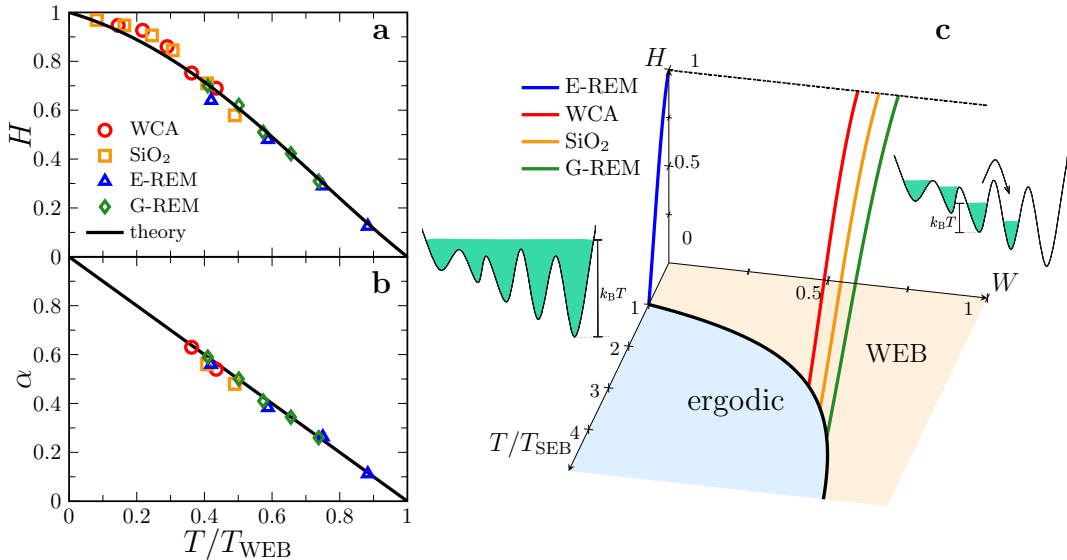


FIG. 7. Unified phase diagram of activated aging and WEB in glasses. (a) WEB order parameter H and (b) power-law convergence exponent α obtained by simulations of four glass models ($w = t/t_w = 1/2$). The theoretical lines are Eqs. (2) and (6). (c) In the unified phase diagram, WEB and ergodic phases are separated by the $T/T_{\text{SEB}} = 1/(1 - W)$ line, and the H -axis quantifies the order parameter. Each glass model corresponds to one line in the plot with the corresponding W . Insets are schematic energy landscapes in ergodic and WEB phases; the arrow indicates hopping to lower energy basins during aging.

Table 1. Characteristic temperatures. The spin glass transition temperature T_c is obtained by thermodynamic calculations for G-REM [33] and E-REM [55]. The divergence temperature T_0 is estimated from the VFT fitting of the α -relaxation time $\tau_{\text{eq}} \sim \exp\left(\frac{C}{T-T_0}\right)$ for the WCA model [56]. The MCT temperature T_{MCT} is estimated from the MCT fitting, $\tau_{\text{eq}} \sim (T - T_{\text{MCT}})^{-\gamma}$ for the WCA model [57], and $D \sim (T - T_{\text{MCT}})^\gamma$ of the diffusion constant D for amorphous SiO_2 [58]. The onset temperature T_{onset} in the WCA model corresponds to the crossover temperature where the Stokes-Einstein relation, $\tau_{\text{eq}} \sim D^{-1}$, breaks down [59]. Using four different criteria, Ref. [60] reports $T_{\text{onset}} = 0.6 - 0.7$ for the WCA model. Data without references are obtained by the current study (see the main text and SM Sec. S4 for details).

	T_c	T_0	T_{MCT}	T_{onset}	T_K	T_{WEB}	W
G-REM	$\frac{1}{\sqrt{2 \log 2}}$ [33]	-	-	-	-	3.05	0.722
E-REM 1 [55]	-	-	-	-	-	1	1
WCA	-	0.158 [56]	0.28 [57]	0.513 [59] 0.6-0.7 [60]	0.21	0.69	0.594
SiO_2	-	-	3330K [58]	5800K	-	9800K	0.66

Fig. 5(a,d), the high- T simulation results can be fitted to the form, $F_w(t_w) = \tilde{H}(1 + A t_w^{-\alpha}) - k \ln t_w$, from which \tilde{H} and α are obtained. Note that this expression only works in the intermediate- t_w regime (see Eq. 5), and thus the small- t_w (microscopic dynamics) and large- t_w (thermalization) data points should be excluded from the fitting. At lower T , a dip in $F_w(t_w)$, which might be attributed to the so-called boson peak [63], appears after the short-time processes, making the above fitting form inapplicable. Nevertheless, at these temperatures, \tilde{H} can still be estimated since the plateau is well-defined. Then the relation $H = \tilde{H}/f$ is used to estimate H (see SM Sec. S4 for the data of f). The values of H and α are plotted in Fig. 7(a,b), as functions of $\hat{x} = T/T_{\text{WEB}}$ with a fixed $w = 1/2$. With a proper choice of T_{WEB} , these data collapse with the GTM the-

oretical curves Eq. (2) and (6). Note that T_{WEB} is obtained from fitting the data to the arcsin law Eq. (2). A further consistent check is illustrated in Fig. 1d for the WCA model: using the same T_{WEB} and f , the theoretical curve $\tilde{H}(w, \hat{x} = 0.36) = fH(w, \hat{x} = 0.36)$, with H given by Eq. (2), agrees with the simulation data $F^{\text{ag}}(w)$. Together, Fig. 1d and 7(a,b) suggest that the theory works for different T and $w = t/t_w$.

The finite-size dependence of the coefficient k in the logarithmic term $-k \ln t_w$ reveals very interesting properties of activated processes. According to Eq. (5), we expect $k \sim 1/N$ in mean-field models. This N essentially appears in the Gaussian term in Eq. (3). In non-mean-field systems such as the WCA and amorphous silica models, N should be replaced by the size n of clusters involved in the activation events, because n determines the true scale of the energy barrier. Such clusters are also

called “mosaics” in the RFOT [44]. If the system size N is smaller than the characteristic size n , then all particles participate in the activated aging, and $k(N)$ would depend on N . On the other hand, if $N > n$, $k(N)$ would be independent of N because n imposes a cutoff of the relevant size. In other words, the finite-size data $k(N)$ can provide an estimate of the characteristic size n : with an increasing N , the data of $k(N)$ should reach a constant at $N = n$. Furthermore, we can obtain a length scale $\xi_{\text{ag}} \sim n^{1/d}$. Note that ξ_{ag} is a static length scale because it is time-independent. This length essentially reflects properties of the energy landscape, but remarkably, it is extracted from aging dynamics.

Based on the above consideration, we focus on the logarithmic part of the $F_w(t_w)$ data, and perform fitting using the form $F_w(t_w) \sim -k \ln t_w$ (see Fig. 5b,e) to obtain $k(N)$ (see Fig. 5c,f). In the WCA model, $k \sim N^{-\beta}$ with $\beta \approx 0.1 - 0.4$ when $N < n$ (see SM Sec. S4), and $k \sim \text{constant}$ when $N > n$. From these data, the characteristic size n and length $\xi_{\text{ag}} \equiv \frac{1}{2}(n/\rho)^{1/3}$ are determined. Note that there is no adjustable parameter in the definition of ξ_{ag} - the coefficient $1/2$ follows the convention that the static length is defined as a half of the box length. In the amorphous silica model, the plateau in $k(N)$ is not observed within the largest simulated system size. This difference is very interesting, because it highlights the distinct nature of the activation energy in the two models. In large WCA systems ($N > n$), the barrier energy $\Delta E[n(T)]$ is determined by the T -dependent $n(T)$ (note that $n(T)$ grows with a decreasing T), but not the system size N . In contrast, in the amorphous silica model $\Delta E(N)$ depends only on N , which suggests that ΔE is a T -independent constant for a given system size. Correspondingly, the equilibrium relaxation time behaves as $\tau_{\text{eq}} \sim \exp[\Delta E(T)/T]$ and $\tau_{\text{eq}} \sim \exp(\Delta E/T)$ in the two models - this is consistent with the well-known fact that WCA and amorphous silica belong to fragile and strong glass formers respectively [64].

Growth of the static length in the WCA model

In Fig. 6, the characteristic length ξ_{ag} in the WCA model is compared to two other static lengths. (i) The first one is the PTS length, ξ_{PTS} , a standard measure of the mosaic size, which scales as $n \sim (\xi_{\text{PTS}})^d$ [41]. In practice, starting from an equilibrium configuration, particles outside a cavity of radius R are pinned. The characteristic decay length ξ_{PTS} is then extracted by measuring how the overlap between the initial and new equilibrium configurations decays as a function of R [65–67]. Thus, ξ_{PTS} quantifies the range of influence exerted by the amorphous boundary. The ξ_{PTS} data plotted in Fig. 6 are obtained from Ref. [42] for the WCA model at the same density $\rho = 1.2$. (ii) The second one is the length scale ξ_{Hessian} used to collapse the data of

the smallest eigenvalue of the Hessian matrix at different T [43], which matches ξ_{PTS} as noticed in Ref. [68]. The length ξ_{Hessian} has been measured for the Kob-Anderson binary Lennard-Jones (KA-LJ) model [43] but not yet for the WCA model. Ref. [42] shows that the PTS lengths, $\xi_{\text{PTS}}(T)$, for the two models (WCA and KA-LJ) collapse if T is rescaled by a factor of $4/3$, $\xi_{\text{PTS}}^{\text{WCA}}(T) = \xi_{\text{PTS}}^{\text{KA-LJ}}(4T/3)$. Based on this observation, in Fig. 6 we plot ξ_{Hessian} of the KA-LJ model from [43] as a function of $3T/4$.

Surprisingly, we find that not only ξ_{Hessian} and ξ_{PTS} collapse on the same curve as expected [68], the length ξ_{ag} also collapses. The growth range of each single length is limited within a factor of $2 \sim 3$, due to different numerical challenges: to obtain ξ_{Hessian} and ξ_{PTS} one needs to equilibrate the system, which is impossible at a low T ; to obtain ξ_{ag} , one needs to fit the logarithmic decay of the aging function (see Fig. 5), which becomes difficult at a high T due to rapid thermalization. However, if we combine the three lengths, the variation covers one decade. We have examined that crystallization and fractionation are absent within the aging dynamics under investigation, and therefore confirmed that the growth of ξ_{ag} is not due to these effects (see SM Sec. S4.).

We can now perform a scaling analysis of the combined ξ data of ξ_{Hessian} , ξ_{PTS} and ξ_{ag} . According to the RFOT, ξ diverges at the Kauzmann temperature (ideal glass transition temperature) T_K , as $\xi \sim (T - T_K)^{-\nu}$, where $\nu = 1/(d - \theta) = 2/d = 2/3$, with $\theta = d/2$ the surface tension exponent and $d = 3$ the dimensionality [44, 45]. The best fitting of the data in Fig. 6 gives $T_K \approx 0.21$ and $\nu = 0.61(1)$. The estimated Kauzmann temperature $T_K \approx 0.21$ is above, but not far away from, the reported divergence temperature $T_0 = 0.158$ of the relaxation time $\tau_{\text{eq}} \sim \exp(\frac{C_0}{T - T_0})$ obtained by the Vogel–Fulcher–Tamann (VFT) fitting [56]. The exponent $\nu = 0.61(1)$ is consistent with the value $\nu = 2/3$ given by the theoretical argument [44, 45]. The data do not support the possibility of diverging $\xi(T)$ at $T_K = 0$ following a power-law (Fig. 6-inset).

In a recent study, the PTS length ξ_{PTS} is estimated for hard spheres (HSs) in an unprecedentedly supercooled regime by utilizing an efficient swap MC algorithm, with the Kauzmann point estimated at $Z_K \approx 45$ by extrapolating the vanishing point of the configurational entropy [50]. An analogy has also been suggested between $1/T$ in molecular systems and the reduced pressure (also called compressibility factor) $Z = P/(\rho T)$ in HSs, by showing the data collapse of the relaxation time as a function of $1/T$ in the former and Z in the latter [69, 70]. Inspired by this analogy, in Fig. 6, we include the data of ξ_{PTS} for HSs. Very interestingly, if ξ is rescaled by the value $\xi(T_{\text{MCT}})$ at the MCT crossover, and then plotted as a function of $(T - T_K)/(T_{\text{MCT}} - T_K)$ for the WCA model, and of $(Z^{-1} - Z_K^{-1})/(Z_{\text{MCT}}^{-1} - Z_K^{-1})$ for the HS model, all data collapse on the same curve. The additional data from HSs thus strengthen the above analysis following the RFOT scaling.

Universal behavior and a unified phase diagram of aging

The above aging data of spin and structural glasses can be universally described by the same theoretical framework. The WEB temperature T_{WEB} is a model-dependent parameter (see Table 1). With a given w , the WEB order parameter H and exponent α in Eq. (5), obtained from four different models, collapse onto the same theoretical curves given by Eq. (2) and (6), as functions of $\hat{x} = T/T_{\text{WEB}}$ (see Fig. 7a,b).

Figure 7c is a unified phase diagram for the aging behavior in spin and structural glasses. The ergodicity in equilibrium dynamics breaks down at T_{SEB} ($T_{\text{SEB}} = T_c$ in REMs, and $T_{\text{SEB}} = T_{\text{MCT}}$ in structural glasses). The ratio between T_{WEB} and T_{SEB} is specified by the model-dependent parameter W , $T_{\text{WEB}}/T_{\text{SEB}} = 1/(1 - W)$ (see Eq. 4). Each model corresponds to a line in Fig. 7c with a fixed W ; the WEB occurs at $T = T_{\text{WEB}}$, where the order parameter vanishes, $H = 0$. The boundary between ergodic and WEB phases in the $T/T_{\text{SEB}} - W$ plane is defined by the line of $T/T_{\text{SEB}} = 1/(1 - W)$ (i.e., $T = T_{\text{WEB}}$). In Table 1, the values of relevant parameters are summarized for the four models studied; among the listed characteristic temperatures, T_{WEB} appears to be the highest one. We expect that this phase diagram can generally include many other glass systems.

DISCUSSION

In the present work, aging dynamics of several spin and structural glasses are studied under a unified framework built on the GTM. According to the replica theory [1], these models belong to the universality class of 1-RSB. In the future, it will be interesting to generalize the present approach to glass systems that have a hierarchical energy landscape (full-step replica symmetry breaking universality class) [23], such as the Sherrington-Kirkpatrick spin glass model [71] and hard sphere glasses in the Gardner phase [72–74].

In this study, we focus on the temperature regime where activation governs aging dynamics. Our preliminary simulation results of structural glasses suggest that, at very low temperatures, the activation-dominated logarithmic energy decay is switched to a mean-field-like power-law decay [17, 75]. A complete picture should be based on a more systematic exploration of the competition between activated and mean-field aging [76].

As a phenomenological model, the landscape-based GTM is unnecessarily incompatible with other mechanisms based on microscopic properties or processes. For example, the origin of the barrier energy distribution

$P(\Delta E)$ could be related to the pinning energy of domain walls [77], the energy required to flip a domain of spins in kinetically constrained models [78], or the activation energy for local rearrangements of particles [62]. How to reconcile the current landscape interpretation with microscopic mechanisms will be left for future investigations.

It is particularly instructive to compare the current GTM with facilitated trap models (FTMs) [79–81]. The FTM proposed in Refs. [80, 81] describes equilibrium dynamics governed by a distribution of energy barriers (trap energies), $P_{\text{eq}}(T, \Delta E) \propto P(\Delta E) \exp(\Delta E/T)$, where $P(\Delta E)$ is the T -independent distribution determined by the energy landscape. When a facilitation rule is incorporated into the hopping processes under the constraint of a fixed $P_{\text{eq}}(T, \Delta E)$, the trap energies of deep traps effectively diffuse. This diffusion introduces a cut-off time scale τ_p to the trapping time distribution $\psi(\tau)$, even if the original distribution (without facilitation) is unbounded. In contrast, the cutoff time scale $\tau_\alpha^0(n)$ in the GTM has a fundamentally different, purely thermodynamic origin (the superscript “0” indicates that $\tau_\alpha^0(n)$ should be estimated without facilitation). It is determined by the typical size n of the activation clusters, corresponding to the mosaic size in the RFOT scenario. Consequently, the actual equilibrium (α -) relaxation time τ_{eq} in systems like the WCA model should be the minimum of τ_p and $\tau_\alpha^0(n)$; that is, relaxation proceeds via the faster of the two mechanisms (facilitation or RFOT). The influence of facilitation on non-equilibrium aging dynamics, however, remains less clear. In this case, the condition of a fixed $P_{\text{eq}}(T, \Delta E)$ no longer applies, and it is unknown whether facilitation would similarly introduce a cutoff time scale through the diffusion of deep trap energies.

The discussed aging phenomenon is relevant to many other disordered systems. The two-time correlation functions of metallic glasses measured by the X-ray photon correlation spectroscopy [82] can be analyzed to compare with our theoretical predictions. Studies on the non-equilibrium inter-domain dynamics of single protein molecules report a power-law dependence of the characteristic relaxation time τ_c on the observation time t , $\tau_c \sim t^{0.9}$ [83], very close to the linear relationship $\tau_{\text{neq}} \sim t_w$ observed in Fig. 1b. Finally, in the training dynamics of deep learning, the logarithmic decay of energy (loss function), similar to Fig. 1a, is found to be responsible for the gain of generalization ability, in a recently developed thermal deep learning machine [84]. Generalization of the current approach to these systems is expected in the future.

MATERIALS AND METHODS

A. Random energy models

1. Model. A REM comprises 2^N configurations.

Each configuration consists of N Ising spins, whose energy is drawn randomly from a Gaussian probability distribution,

$$\rho_{\text{Gauss}}(E) = \frac{1}{\sqrt{2\pi N}} \exp(-E^2/2N). \quad (7)$$

This original version with the Gaussian distribution $\rho_{\text{Gauss}}(E)$ is called a Gaussian random energy model (G-REM). An alternative version, called an exponential random energy model (E-REM) [38, 55], has been introduced previously, with $\rho_{\text{Gauss}}(E)$ replaced by

$$\rho_{\text{exp}}(E) = \frac{1}{T_c} \exp(E/T_c) \Theta(-E), \quad (8)$$

where $\Theta(x)$ is the Heaviside step function. In each realization, the energy assignment of 2^N configurations is fixed (quenched disorder) in the following static barrier-tree analyses and dynamical simulations. The procedure is then repeated for $\sim 1000 - 20000$ realizations to take the statistical average.

2. Searching for landscape basins and barriers: barrier-tree algorithm. The BT algorithm searches for all local minima and saddle points in the energy landscape, and organizes them into a barrier tree (see Fig. 3a for an example of a sub-tree). A spin configuration is referred to as a local minimum if its energy is lower than the energy of any adjacent configuration (each configuration has N adjacent configurations related by a single spin flip). The complete set of local minima are found by exhaustive search. To find the saddle point between two local minima, the algorithm first searches for all possible paths (a path is a series of subsequent spin flips) between the two minima, with the maximum energy point identified along each path – the saddle point is then defined as the lowest energy point among all maxima (min-max).

The barrier tree is constructed recursively in the following way: (i) find all N_b local minima; (ii) connect the two lowest local minima by a saddle point, and replace this sub-tree with a new node whose energy is equivalent to the saddle point energy (the new set has $N_b - 1$ nodes); (iii) repeat (i) and (ii) until only one node is left in the set ($N_b = 1$). More details about the algorithm can be found in Refs. [51–54].

As shown in Fig. 3a, generally a local minimum can be connected to multiple saddle points. For a given local minimum with an energy E_{lm} , we define E_{sp} as the lowest energy of its connected saddle points, and the barrier energy is given by $\Delta E = E_{\text{sp}} - E_{\text{lm}}$. Our definition of ΔE is also consistent with the above min-max definition of saddle points. In this way, each local minimum is assigned to an energy barrier ΔE . The probability distribution of ΔE gives $p^{\text{BT}}(\Delta E)$.

Each glass basin corresponds to a local minimum and a saddle point defined in the above way. A glass basin also contains other configurations that are neither local minima nor saddle points – they form a set of configurations connected to the local minimum whose energies

are all below E_{sp} . Numerically, we start from the given local minimum, and search for its direct neighbours with a single-spin flip, the neighbours of neighbours, ..., until the configuration's energy E is larger than E_{sp} . In this way, for a given realization of the REM with a finite N , we find all $i = 1, 2, \dots, N_b$ basins. Each basin corresponds to a set \mathcal{B}_i of configurations belonging to it, a local minimum energy E_{lm}^i , a saddle point energy E_{sp}^i , and a barrier energy $\Delta E_i = E_{\text{sp}}^i - E_{\text{lm}}^i$. Note that many configurations do not belong to any basins.

3. Simulations of single-spin flip Metropolis dynamics: Monte Carlo algorithm. Dynamical trajectories, which are time sequences of configurations $\mathcal{C}(t)$, are obtained by standard single-spin flip MC simulations, starting from random initial configurations. An example is provided in Fig. S6a, where the energy $E(t_w)$ of the configuration at t_w is plotted. In order to obtain the aging function $\Pi_w(t_w)$, our task is to transform the configuration trajectory to a basin trajectory (Fig. S6b). The detailed procedure is described below.

During the dynamics, the system is in the basin \mathcal{B}_i if $\mathcal{C}(t) \in \mathcal{B}_i$ and it leaves the basin if $\mathcal{C}(t) \notin \mathcal{B}_i$ anymore. The duration in the basin defines the hopping time (trapping time) τ . In this way, we identify a sequence of hopping events with $\{\tau_k, E_{\text{lm}}^{i_k}, E_{\text{sp}}^{i_k}, \Delta E_{i_k}\}$, where $k = 1, 2, \dots$ and $1 \leq i_k \leq N_b$ denotes that the k -th event is in the basin i_k . Note that the transient time between basins is negligible, i.e., we assume that once the system leaves a basin, it immediately falls into the next basin.

A major computational challenge is the exponential growth of the size $\mathcal{O}(2^N)$ of the configuration space with the system size N . For systems with $N > 20$ spins, storing the entire landscape would exceed the memory limit of standard computers. To address this issue, we only save the portion of the landscape that is actually explored during the MC dynamical simulations. This trick allows us to simulate up to $N = 128$ spins for maximally 10^9 MC steps, with 1 GB memory.

B. Weeks-Chandler-Andersen model

1. Model. The WCA model is an 80 : 20 binary mixture of type A and type B particles interacting with the Lennard-Jones (LJ) potential,

$$V(r) = 4\epsilon_{\alpha\beta} \left[\left(\frac{r}{\sigma_{\alpha\beta}} \right)^{12} - \left(\frac{r}{\sigma_{\alpha\beta}} \right)^6 \right], \quad (9)$$

where $\alpha, \beta \in \{A, B\}$, with parameters $\sigma_{AB}/\sigma_{AA} = 0.8$, $\sigma_{BB}/\sigma_{AA} = 0.88$, $\epsilon_{AB}/\epsilon_{AA} = 1.5$, and $\epsilon_{BB}/\epsilon_{AA} = 0.5$. The pair potential $V(r)$ is truncated and shifted to zero at the minimum, $r_{\alpha\beta}^{\text{cut}} = 2^{1/6} \sigma_{\alpha\beta}$. All particles have the same unit mass, $m_A = m_B = m$. The parameters ϵ_{AA} , σ_{AA} and $\sqrt{m\sigma_{AA}^2/\epsilon_{AA}}$ are used as the energy, length, and time units. The presented data are obtained for large (type A) particles.

2. Molecular dynamics simulation method. Simulations of the WCA model are performed at a fixed

number density $\rho = 1.2$. The MCT temperature at this density is $T_{\text{MCT}} \approx 0.28$ [59]. We generate equilibrium configurations at an initial temperature $T_{\text{eq}} = 5.0$, and then instantly quench the samples to a target temperature T . To suppress the wild temperature fluctuations at the initial stage, the aging simulations are performed under the isokinetic ensemble, a variant of the canonical ensemble [85]. The temperature (kinetic energy) is rescaled to the target temperature every 10000 MD steps (100 LJ time units).

C. Amorphous silica model

1. Model. The atomic interactions in the amorphous silica (SiO_2) is modeled by the Beest Kramer van Santen (BKS) potential, derived from ab initio calculations and lattice dynamics calculations [86]. The BKS potential for both Si – O and O – O interactions diverges to negative infinity at a small distance r , leading to unrealistic attractions at high temperatures. To address this issue, the BKS potential at small distances is replaced by a harmonic repulsive potential, which gives the interactions in the following form:

$$V(r) = \begin{cases} D_{\alpha\beta}(r - r_{\alpha\beta}^c)^2, & r < r_{\alpha\beta}^c, \\ \frac{q_\alpha q_\beta e^2}{r} + A_{\alpha\beta} \exp(-B_{\alpha\beta}r) - \frac{C_{\alpha\beta}}{r^6}, & r \geq r_{\alpha\beta}^c, \end{cases}$$

where $\alpha, \beta \in \{\text{Si}, \text{O}\}$. The parameters of BKS potential can be found in the standard reference [86]. For the harmonic potential, $D_{\alpha\beta} = 100$, $r_{\text{OO}}^c = 1.43869$ and $r_{\text{SiO}}^c = 1.19362$. The Coulomb interaction is computed using the Ewald method. All quantities are expressed in metal units.

2. Molecular dynamics simulation method.

The MD simulations are carried out using the Large-scale Atomic/Molecular Massively Parallel Simulator (LAMMPS) [87], at a constant volume with a fixed mass density $\rho_m = 2.36 \text{ g/cm}^3$. The Verlet algorithm with a time step of 1.6 fs is used to integrate the equations of motion. We simulate the aging dynamics by quenching the system from a high initial temperature $T_{\text{eq}} = 8000 \text{ K}$ to a low target temperature T . The initial equilibrium configurations at T_{eq} are melted from a crystalline SiO_2 in the NVT ensemble. After quenching, the aging dynamics are simulated with velocities rescaled every 50 steps to keep the target temperature T .

[1] M. Mézard, G. Parisi, and M. A. Virasoro, *Spin glass theory and beyond: An Introduction to the Replica Method and Its Applications*, Vol. 9 (World Scientific Publishing Company, 1987).

[2] G. Parisi, P. Urbani, and F. Zamponi, *Theory of simple glasses: exact solutions in infinite dimensions* (Cambridge University Press, 2020).

[3] L. C. E. Struik *et al.*, *Physical aging in amorphous polymers and other materials*, Vol. 106 (Citeseer, 1978).

[4] R. E. Courtland and E. R. Weeks, Direct visualization of ageing in colloidal glasses, *Journal of Physics: Condensed Matter* **15**, S359 (2002).

[5] P. A. Gago and S. Boettcher, Universal features of annealing and aging in compaction of granular piles, *Proceedings of the National Academy of Sciences* **117**, 33072 (2020).

[6] G. Janzen and L. M. Janssen, Aging in thermal active glasses, *Physical Review Research* **4**, L012038 (2022).

[7] M. Baity-Jesi, L. Sagun, M. Geiger, S. Spigler, G. B. Arous, C. Cammarota, Y. LeCun, M. Wyart, and G. Biroli, Comparing dynamics: Deep neural networks versus glassy systems, in *International Conference on Machine Learning* (PMLR, 2018) pp. 314–323.

[8] F. H. Stillinger, *Energy landscapes, inherent structures, and condensed-matter phenomena* (Princeton University Press, 2015).

[9] J.-P. Bouchaud and M. Mézard, Aging in glasses: Traps and mode-coupling theory, *Progress of Theoretical Physics Supplement* **126**, 181 (1997).

[10] L. F. Cugliandolo, Dynamics of glassy systems, in *Slow Relaxations and nonequilibrium dynamics in condensed matter*, edited by J.-L. Barrat, M. Feigelman, J. Kurchan, and J. Dalibard (Springer Berlin Heidelberg, Berlin, Heidelberg, 2003) pp. 367–521.

[11] F. Arceri, F. P. Landes, L. Berthier, and G. Biroli, Glasses and aging, a statistical mechanics perspective on, in *Statistical and Nonlinear Physics* (Springer, 2022) pp. 229–296.

[12] L. F. Cugliandolo and J. Kurchan, Analytical solution of the off-equilibrium dynamics of a long-range spin-glass model, *Physical Review Letters* **71**, 173 (1993).

[13] L. F. Cugliandolo and P. Le Doussal, Large time nonequilibrium dynamics of a particle in a random potential, *Physical Review E* **53**, 1525 (1996).

[14] A. Altieri, G. Biroli, and C. Cammarota, Dynamical mean-field theory and aging dynamics, *Journal of Physics A: Mathematical and Theoretical* **53**, 375006 (2020).

[15] L. F. Cugliandolo and J. Kurchan, On the out-of-equilibrium relaxation of the Sherrington-Kirkpatrick model, *Journal of Physics A: Mathematical and General* **27**, 5749 (1994).

[16] M. Bernaschi, A. Billoire, A. Maiorano, G. Parisi, and F. Ricci-Tersenghi, Strong ergodicity breaking in aging of mean-field spin glasses, *Proceedings of the National Academy of Sciences* **117**, 17522 (2020).

[17] G. Folena, S. Franz, and F. Ricci-Tersenghi, Rethinking mean-field glassy dynamics and its relation with the energy landscape: The surprising case of the spherical mixed p-spin model, *Physical Review X* **10**, 031045 (2020).

[18] G. Folena and F. Zamponi, On weak ergodicity breaking in mean-field spin glasses, *SciPost Physics* **15**, 109 (2023).

[19] J. Kurchan and L. Laloux, Phase space geometry and slow dynamics, *Journal of Physics A: Mathematical and General* **29**, 1929 (1996).

[20] J.-P. Bouchaud, L. F. Cugliandolo, J. Kurchan, and M. Mézard, Out of equilibrium dynamics in spin-glasses and other glassy systems, *Spin glasses and random fields* **12**, 161 (1998).

[21] E. Agoritsas, T. Maimbourg, and F. Zamponi, Out-of-equilibrium dynamical equations of infinite-dimensional particle systems i. the isotropic case, *Journal of Physics A: Mathematical and Theoretical* **52**, 144002 (2019).

[22] J.-P. Bouchaud, Weak ergodicity breaking and aging in disordered systems, *Journal de Physique I* **2**, 1705 (1992).

[23] J.-P. Bouchaud and D. S. Dean, Aging on paris's tree, *Journal de Physique I* **5**, 265 (1995).

[24] M. Goldstein, Viscous liquids and the glass transition: a potential energy barrier picture, *The Journal of Chemical Physics* **51**, 3728 (1969).

[25] P. G. Debenedetti and F. H. Stillinger, Supercooled liquids and the glass transition, *Nature* **410**, 259 (2001).

[26] A. J. Bray, Theory of phase-ordering kinetics, *Advances in Physics* **43**, 357 (1994).

[27] D. S. Fisher and D. A. Huse, Ordered phase of short-range Ising spin-glasses, *Physical review letters* **56**, 1601 (1986).

[28] A. Bray and M. Moore, Lower critical dimension of Ising spin glasses: a numerical study, *Journal of Physics C: Solid State Physics* **17**, L463 (1984).

[29] P. Mayer and P. Sollich, Ageing in one-dimensional coagulation-diffusion processes and the Fredrickson-Andersen model, *Journal of Physics A: Mathematical and Theoretical* **40**, 5823 (2007).

[30] J.-P. Bouchaud and A. Georges, Anomalous diffusion in disordered media: statistical mechanisms, models and physical applications, *Physics reports* **195**, 127 (1990).

[31] C. Li, H. Liu, and X. Xie, Route of random process to ultraslow aging phenomena, *Physical Review Letters* **134**, 197102 (2025).

[32] D. J. Gross and M. Mézard, The simplest spin glass, *Nuclear Physics B* **240**, 431 (1984).

[33] B. Derrida, Random-energy model: Limit of a family of disordered models, *Physical Review Letters* **45**, 79 (1980).

[34] J. Černý and T. Wassmer, Aging of the Metropolis dynamics on the random energy model, *Probability Theory and Related Fields* **167**, 253 (2017).

[35] V. Gayrard, Aging in Metropolis dynamics of the REM: a proof, *Probability Theory and Related Fields* **174**, 501 (2019).

[36] V. Gayrard and L. Hartung, Dynamic phase diagram of the REM, in *Statistical Mechanics of Classical and Disordered Systems: Luminy, France, August 2018* (Springer, 2019) pp. 111–170.

[37] B. Derrida, P. Mottishaw, and V. Gayrard, Random energy models: broken replica symmetry and activated dynamics, in *Spin Glass Theory and Far Beyond: Replica Symmetry Breaking after 40 Years* (World Scientific, 2023) pp. 657–677.

[38] M. Baity-Jesi, G. Biroli, and C. Cammarota, Activated aging dynamics and effective trap model description in the random energy model, *Journal of Statistical Mechanics: Theory and Experiment* **2018**, 013301 (2018).

[39] D. A. Stariolo and L. F. Cugliandolo, Activated dynamics of the Ising p-spin disordered model with finite number of variables, *Europhysics Letters* **127**, 16002 (2019).

[40] R. A. Denny, D. R. Reichman, and J.-P. Bouchaud, Trap models and slow dynamics in supercooled liquids, *Physical review letters* **90**, 025503 (2003).

[41] J.-P. Bouchaud and G. Biroli, On the Adam-Gibbs-Kirkpatrick-Thirumalai-Wolynes scenario for the viscosity increase in glasses, *The Journal of chemical physics* **121**, 7347 (2004).

[42] G. M. Hocky, T. E. Markland, and D. R. Reichman, Growing point-to-set length scale correlates with growing relaxation times in model supercooled liquids, *Physical review letters* **108**, 225506 (2012).

[43] S. Karmakar, E. Lerner, and I. Procaccia, Direct estimate of the static length-scale accompanying the glass transition, *Physica A: Statistical Mechanics and its Applications* **391**, 1001 (2012).

[44] T. R. Kirkpatrick, D. Thirumalai, and P. G. Wolynes, Scaling concepts for the dynamics of viscous liquids near an ideal glassy state, *Physical Review A* **40**, 1045 (1989).

[45] V. Lubchenko and P. G. Wolynes, Theory of structural glasses and supercooled liquids, *Annu. Rev. Phys. Chem.* **58**, 235 (2007).

[46] W. Kob and J.-L. Barrat, Aging effects in a Lennard-Jones glass, *Physical review letters* **78**, 4581 (1997).

[47] G. B. Arous and J. Černý, Course 8 dynamics of trap models, *Mathematical statistical physics, Ecole d'Été de physique des houches session LXXXIII*, 331 (2006).

[48] V. Gayrard, Convergence of clock processes and aging in Metropolis dynamics of a truncated REM, in *Annales Henri Poincaré*, Vol. 17 (Springer, 2016) pp. 537–614.

[49] E. Fermi, P. Pasta, S. Ulam, and M. Tsingou, *Studies of the nonlinear problems*, Tech. Rep. (Los Alamos National Laboratory (LANL), Los Alamos, NM (United States), 1955).

[50] L. Berthier, P. Charbonneau, D. Coslovich, A. Ninarello, M. Ozawa, and S. Yaida, Configurational entropy measurements in extremely supercooled liquids that break the glass ceiling, *Proceedings of the National Academy of Sciences* **114**, 11356 (2017).

[51] C. Flamm, W. Fontana, I. L. Hofacker, and P. Schuster, Rna folding at elementary step resolution, *Rna* **6**, 325 (2000).

[52] F. F. Ferreira, J. F. Fontanari, and P. F. Stadler, Landscape statistics of the low-autocorrelation binary string problem, *Journal of Physics A: Mathematical and General* **33**, 8635 (2000).

[53] J. F. Fontanari and P. F. Stadler, Fractal geometry of spin-glass models, *Journal of Physics A: Mathematical and General* **35**, 1509 (2002).

[54] C. Flamm, I. L. Hofacker, P. F. Stadler, and M. T. Wolfinger, Barrier trees of degenerate landscapes, (2002).

[55] J.-P. Bouchaud and M. Mézard, Universality classes for extreme-value statistics, *Journal of Physics A: Mathematical and General* **30**, 7997 (1997).

[56] L. Wang and N. Xu, Probing the glass transition from structural and vibrational properties of zero-temperature glasses, *Phys. Rev. Lett.* **112**, 055701 (2014).

[57] L. Berthier and G. Tarjus, Critical test of the mode-coupling theory of the glass transition, *Phys. Rev. E* **82**, 031502 (2010).

[58] J. Horbach and W. Kob, Static and dynamic properties

of a viscous silica melt, *Phys. Rev. B* **60**, 3169 (1999).

[59] L. Berthier and G. Tarjus, The role of attractive forces in viscous liquids, *The Journal of Chemical Physics* **134**, 214503 (2011).

[60] A. Banerjee, M. K. Nandi, S. Sastry, and S. Maitra Bhattacharyya, Determination of onset temperature from the entropy for fragile to strong liquids, *The Journal of chemical physics* **147** (2017).

[61] A. Heuer, Exploring the potential energy landscape of glass-forming systems: from inherent structures via metabasins to macroscopic transport, *Journal of Physics: Condensed Matter* **20**, 373101 (2008).

[62] W. Ji, M. Pica Ciamarra, and M. Wyart, The role of excitations in supercooled liquids: Density, geometry, and relaxation dynamics, *Proceedings of the National Academy of Sciences* **122**, e2416800122 (2025).

[63] J. Habasaki, I. Okada, and Y. Hiwatari, Origins of the two-step relaxation and the boson peak in an alkali silicate glass studied by molecular-dynamics simulation, *Physical Review E* **52**, 2681 (1995).

[64] L. Berthier and G. Biroli, Theoretical perspective on the glass transition and amorphous materials, *Reviews of Modern Physics* **83**, 587 (2011).

[65] G. Biroli, J.-P. Bouchaud, A. Cavagna, T. S. Grigera, and P. Verrocchio, Thermodynamic signature of growing amorphous order in glass-forming liquids, *Nature Physics* **4**, 771 (2008).

[66] W. Kob, S. Roldán-Vargas, and L. Berthier, Non-monotonic temperature evolution of dynamic correlations in glass-forming liquids, *Nature Physics* **8**, 164 (2012).

[67] S. Yaida, L. Berthier, P. Charbonneau, and G. Tarjus, Point-to-set lengths, local structure, and glassiness, *Physical Review E* **94**, 032605 (2016).

[68] S. Karmakar, C. Dasgupta, and S. Sastry, Length scales in glass-forming liquids and related systems: a review, *Reports on Progress in Physics* **79**, 016601 (2015).

[69] O. Dauchot, F. Ladieu, and C. P. Royall, The glass transition in molecules, colloids and grains: universality and specificity, *Comptes Rendus. Physique* **24**, 25 (2023).

[70] L. Ortlieb, T. S. Ingebrigtsen, J. E. Hallett, F. Turci, and C. P. Royall, Probing excitations and cooperatively rearranging regions in deeply supercooled liquids, *Nature Communications* **14**, 2621 (2023).

[71] D. Sherrington and S. Kirkpatrick, Solvable model of a spin-glass, *Physical review letters* **35**, 1792 (1975).

[72] P. Charbonneau, J. Kurchan, G. Parisi, P. Urbani, and F. Zamponi, Fractal free energy landscapes in structural glasses, *Nature communications* **5**, 3725 (2014).

[73] L. Berthier, P. Charbonneau, Y. Jin, G. Parisi, B. Seoane, and F. Zamponi, Growing timescales and lengthscales characterizing vibrations of amorphous solids, *Proceedings of the National Academy of Sciences* **113**, 8397 (2016).

[74] P. Urbani, Y. Jin, and H. Yoshino, The gardner glass, in *Spin glass theory and far beyond: replica symmetry breaking after 40 years* (World Scientific, 2023) pp. 219–238.

[75] Y. Nishikawa, M. Ozawa, A. Ikeda, P. Chaudhuri, and L. Berthier, Relaxation dynamics in the energy landscape of glass-forming liquids, *Physical Review X* **12**, 021001 (2022).

[76] M. R. Carbone and M. Baity-Jesi, Competition between energy-and entropy-driven activation in glasses, *Physical Review E* **106**, 024603 (2022).

[77] T. Nattermann and J. Villain, Random-field Ising systems: A survey of current theoretical views, *Phase transitions* **11**, 5 (1988).

[78] P. Sollich and M. R. Evans, Glassy time-scale divergence and anomalous coarsening in a kinetically constrained spin chain, *Physical review letters* **83**, 3238 (1999).

[79] J.-P. Bouchaud, A. Comtet, and C. Monthus, On a dynamical model of glasses, *Journal de Physique I* **5**, 1521 (1995).

[80] C. Scalliet, B. Guiselin, and L. Berthier, Excess wings and asymmetric relaxation spectra in a facilitated trap model, *The Journal of Chemical Physics* **155** (2021).

[81] B. Guiselin, C. Scalliet, and L. Berthier, Microscopic origin of excess wings in relaxation spectra of supercooled liquids, *Nature Physics* **18**, 468 (2022).

[82] X. Zhang, H. Lou, B. Ruta, Y. Chushkin, F. Zontone, S. Li, D. Xu, T. Liang, Z. Zeng, H.-k. Mao, *et al.*, Pressure-induced nonmonotonic cross-over of steady relaxation dynamics in a metallic glass, *Proceedings of the National Academy of Sciences* **120**, e2302281120 (2023).

[83] X. Hu, L. Hong, M. Dean Smith, T. Neusius, X. Cheng, and J. C. Smith, The dynamics of single protein molecules is non-equilibrium and self-similar over thirteen decades in time, *Nature Physics* **12**, 171 (2016).

[84] G. Huang, L. S. Chan, H. Yoshino, G. Zhang, and Y. Jin, Liquid and solid layers in a thermal deep learning machine, *arXiv preprint arXiv:2506.06789* (2025).

[85] M. E. Tuckerman, *Statistical Mechanics: Theory and Molecular Simulation*, reprinted (with corr.) ed., Oxford Graduate Texts (Oxford Univ. Press, Oxford, 2015).

[86] B. Van Beest, G. J. Kramer, and R. Van Santen, Force fields for silicas and aluminophosphates based on ab initio calculations, *Physical review letters* **64**, 1955 (1990).

[87] A. P. Thompson, H. M. Aktulga, R. Berger, D. S. Bolineanu, W. M. Brown, P. S. Crozier, P. J. In't Veld, A. Kohlmeyer, S. G. Moore, T. D. Nguyen, *et al.*, Lammps-a flexible simulation tool for particle-based materials modeling at the atomic, meso, and continuum scales, *Computer physics communications* **271**, 108171 (2022).

[88] C. Monthus and J.-P. Bouchaud, Models of traps and glass phenomenology, *Journal of Physics A: Mathematical and General* **29**, 3847 (1996).

[89] J. Harland and W. Van Megen, Crystallization kinetics of suspensions of hard colloidal spheres, *Physical Review E* **55**, 3054 (1997).

[90] T. S. Ingebrigtsen, J. C. Dyre, T. B. Schröder, and C. P. Royall, Crystallization instability in glass-forming mixtures, *Physical Review X* **9**, 031016 (2019).

[91] H. E. Stanley, *Phase transitions and critical phenomena* (Clarendon Press, Oxford, 1971).

[92] Y. Brumer and D. R. Reichman, Mean-field theory, mode-coupling theory, and the onset temperature in supercooled liquids, *Physical Review E* **69**, 041202 (2004).

[93] E. Bitzek, P. Koskinen, F. Gähler, M. Moseler, and P. Gumbsch, Structural relaxation made simple, *Physical review letters* **97**, 170201 (2006).

ACKNOWLEDGMENTS

We warmly thank Wenyue Fan, Gang Huang, Wencheng Ji, Walter Kob, Jian Liu, C. Patrick Royall, Yujie Wang,

Hajime Yoshino and Haijun Zhou for discussions.

Funding: Y.J. acknowledges financial support from NSFC (Grants 12161141007, 11935002 and 12047503), from Chinese Academy of Sciences (Grant ZDBS-LY-7017 and KGFZD-145-22-13) and from Wenzhou Institute (Grant WIU- CASQD2023009). D.P. acknowledges support from NSFC (Grants 12404290). In this work access was granted to the High-Performance Computing Cluster of Institute of Theoretical Physics - the Chinese Academy of Sciences.

Author Contributions: All authors contributed equally to this work.

Competing Interests: The authors declare that they have no competing interests.

Data and Materials Availability: All data needed to evaluate the conclusions in the paper are present in the paper and/or the Supplementary Materials. The simulation program is available at <https://doi.org/10.5281/zenodo.17737463>.

Supplemental Material

CONTENTS

Introduction	1
Results	2
Basic aging phenomenon and weak ergodicity breaking	2
Bouchaud's trap model	3
Generalized trap model	5
Aging in spin glass random energy models	7
Aging in structural glasses	8
Growth of the static length in the WCA model	10
Universal behavior and a unified phase diagram of aging	11
Discussion	11
Materials and Methods	11
A. Random energy models	11
B. Weeks-Chandler-Andersen model	12
C. Amorphous silica model	13
References	13
Acknowledgments	15
S1. Aging theory of the generalized trap model	18
A. Outline of the general strategy.	18
B. Long-time power-law convergence to the asymptotic plateau	18
C. Short-time linear decay	20
D. Logarithmic decay due to finite-size effects in the generalized trap model	21
S2. Additional simulation data for the random energy model	24
A. Energy trajectory	24
B. Test of the renewal mechanism	24
C. Verification of the Arrhenius law	25
S3. Thermodynamics of the finite-size random energy model: a tree-expansion theory	26
A. Probability distributions	26
1. The first order: $\Omega = 1$	26
2. The second order: $\Omega = 2$	27
3. The third order: $\Omega = 3$	27
4. Verification with the numerical barrier-tree algorithm	29
B. Internal entropy	29
C. Number of basins	30
S4. Additional simulation data for structural glasses	32
A. Comparison of different simulation algorithms for the WCA model.	32
B. Absence of crystallization and phase separation during aging in the WCA model.	32
C. Estimate of the onset temperature for amorphous silica	33
D. Nonergodicity order parameter	34
E. Exponent β	35

S1. AGING THEORY OF THE GENERALIZED TRAP MODEL

A. Outline of the general strategy.

Our theoretical derivation of the behavior of the aging function $\Pi(t_w, t_w + t)$ follows the strategy provided in Refs. [23, 88]. If the system is trapped in a basin with a trapping time τ , then the probability of the system remaining in the basin after a time t decays exponentially as $\sim e^{-t/\tau}$. According to this, one can write,

$$\Pi(t_w, t_w + t) = \left\langle \sum_{\beta=1}^{N_b} Q(t_w, \tau_\beta) e^{-t/\tau_\beta} \right\rangle = N_b \int_{\tau_0}^{\infty} d\tau Q(t_w, \tau) e^{-t/\tau} \psi(\tau), \quad (\text{S1})$$

where N_b is the total number of basins, $Q(t_w, \tau)$ is the probability of the system being in a basin with a hopping time τ at a waiting time t_w , $\psi(\tau)$ is the hopping time probability distribution function, and τ_0 is the minimum hopping time (in the main text, we have set $\tau_0 = 1$ as the unit of time). The distribution $\psi(\tau)$ is normalized as,

$$\int_{\tau_0}^{\infty} d\tau \psi(\tau) = 1. \quad (\text{S2})$$

In the original Bouchaud's trap model (BTM), the energy barrier distribution is exponential (see Eq. 1). Using the Arrhenius law $\tau(\Delta E) \sim \exp(\Delta E/T)$, the exponential barrier distribution $P(\Delta E) \sim \exp(-\Delta E/T_c)$ can be converted to a power-law hopping time distribution $\psi(\tau)$,

$$\psi(\tau) = x \tau_0^x \tau^{-(1+x)}, \quad (\text{S3})$$

where $x = T/T_c$. Note that Eq. (S3) is normalized according to Eq. (S2).

Bouchaud et al. showed that it is convenient to work in the Laplace transform of $Q(t_w, \tau_\beta)$,

$$\hat{Q}(s, \tau) = \mathcal{L}\{sQ(t_w, \tau)\} = \int_0^{\infty} dt_w e^{-st_w} sQ(t_w, \tau). \quad (\text{S4})$$

When the consecutive hops are independent, the probability $\hat{Q}(s, \tau)$ is [23, 88],

$$\hat{Q}(s, \tau) = \frac{\frac{s\tau}{s\tau+1}}{\mathcal{C} N_b \left\langle \frac{s\tau}{s\tau+1} \right\rangle}, \quad (\text{S5})$$

where \mathcal{C} is a normalization constant. If one considers t_w as an exponentially distributed random variable, as suggested by Eq. (S4), then Eq. (S5) can be understood as $\hat{Q}(s, \tau) \sim \tau/(\tau + \bar{t}_w)$, where the mean waiting time $\bar{t}_w \sim 1/s$. It suggests that the probability of being in a basin with a hopping time τ increases with τ and decreases with the waiting time \bar{t}_w . Let us consider several limiting cases. For any finite τ , $\hat{Q}(s, \tau) \rightarrow 1$ when $\bar{t}_w \rightarrow 0$ (the probability of escaping from any basin is zero without waiting), and $\hat{Q}(s, \tau) \rightarrow 0$ when $\bar{t}_w \rightarrow \infty$ (all basins can be escaped from after long-time waiting). For any finite \bar{t}_w , $\hat{Q}(s, \tau) \rightarrow 0$ when $\tau \rightarrow 0$ (the probability to stay in the basin with $\tau = 0$ is zero), and $\hat{Q}(s, \tau) \rightarrow 1$ when $\tau \rightarrow \infty$ (the basin can not be escaped from if its τ is infinite).

With Eqs. (S1), (S3), (S4) and (S5), the aging function $\Pi(t_w, t_w + t)$ can be obtained. For the generalized trap model (GTM), Eq. (S3) needs to be modified in order to include the finite-size correction, but the other equations can be kept. In the following analyses, the results in Sections. S1 B and S1 C are general for long-time and short-time dynamics in the BTM and GTM, while the logarithmic decay discussed in Section S1 D is uniquely due to the finite-size effects in the GTM.

B. Long-time power-law convergence to the asymptotic plateau

Here we give a theoretical derivation of the second line ($\tau_m < t_w < \tau_{\text{th}}$) in Eq. (5) of the main text. In Eq. (S5), the normalization constant $\mathcal{C} = 1$ in the large-time limit $t_w \rightarrow \infty$. With $\mathcal{C} = 1$, the plateau $H(w, x)$ of the aging function can be determined as given by the arcsin law Eq. (2) (see Fig. S1). In order to obtain the behavior of how the aging function converges to the plateau, it is crucial to consider the next-order $1/t_w$ -correction to \mathcal{C} , as shown below. Note that in this section, we use the BTM distribution Eq. (S3) without finite-size corrections. With Eq. (S3), the average in the denominator of Eq. (S5) becomes,

$$\left\langle \frac{s\tau}{s\tau+1} \right\rangle = \int_{\tau_0}^{\infty} d\tau \frac{s\tau}{s\tau+1} \psi(\tau) = {}_2F_1(1, x; 1+x; -\frac{1}{s\tau_0}), \quad (\text{S6})$$

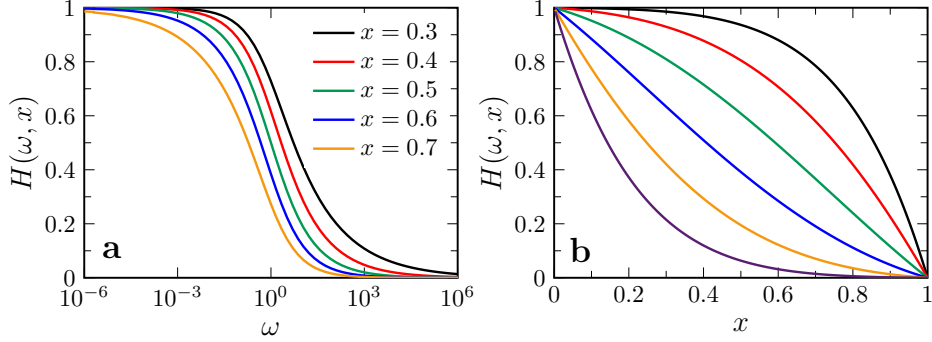


FIG. S1. WEB order parameter $H(w, x)$ by the arcsin law Eq. (2). (a) H versus w for a few different x . (b) H versus x for $\omega = 0.01, 0.1, 0.5, 2, 10, 100$ (top to bottom).

where ${}_2F_1(a, b; c; z)$ is the ordinary hypergeometric function. In the large waiting time limit $t_w \rightarrow \infty$ (or equivalently in the limit $s \rightarrow 0$), ${}_2F_1(1, x; 1 + x; -\frac{1}{s\tau_0}) \approx x\tau_0^x s^x \frac{\pi}{\sin(\pi x)}$. Thus an approximate expression of $\hat{Q}(s, \tau)$ is,

$$\hat{Q}(s, \tau) \approx \frac{\sin(\pi x)\tau_0^{-x}}{CN_b\pi x} \frac{s\tau}{(s\tau + 1)} s^{-x}. \quad (\text{S7})$$

The probability distribution $Q(t_w, \tau)$ can be obtained by performing an inverse Laplace transform to Eq. (S7) and then applying the convolution theorem,

$$Q(t_w, \tau) = \mathcal{L}^{-1} \left\{ \frac{1}{s} \hat{Q}(s, \tau) \right\} \approx \frac{\sin(\pi x)\tau_0^{-x}}{CN_b\pi x\Gamma(x)} \int_0^{t_w} dt' (t_w - t')^{x-1} e^{-t'/\tau}, \quad (\text{S8})$$

where $\Gamma(x)$ is the gamma function. The normalization condition requires that,

$$\left\langle \sum_{\beta} Q(t_w, \tau_{\beta}) \right\rangle = N_b \int_{\tau_0}^{\infty} d\tau Q(t_w, \tau) \psi(\tau) = 1, \quad (\text{S9})$$

or,

$$\mathcal{C} = \frac{\sin(\pi x)}{\pi\Gamma(x)} \times \int_{\tau_0}^{\infty} d\tau \int_0^{t_w} dt' \tau^{-(1+x)} (t_w - t')^{x-1} e^{-t'/\tau}. \quad (\text{S10})$$

Note that \mathcal{C} depends on t_w . Plugging Eqs. (S3) and (S8) into Eq. (S1), we obtain,

$$\begin{aligned} \Pi(t_w, t_w + t) &\approx \frac{\sin(\pi x)}{C\pi\Gamma(x)} \int_0^{\infty} d\tau \int_0^{t_w} dt' \tau^{-(1+x)} (t_w - t')^{x-1} e^{-(t'+t)/\tau} \\ &\approx \frac{\sin(\pi x)}{C\pi} \int_0^{t_w} dt' \left(\frac{t+t'}{t_w - t'} \right)^{-x} (t_w - t')^{-1} \\ &= \frac{\sin(\pi x)}{C\pi} \int_w^{\infty} du u^{-x} (1+u)^{-1}, \end{aligned} \quad (\text{S11})$$

where $u = \frac{t+t'}{t_w - t'}$ and $w = t/t_w$.

To the zeroth order of t_w , Eq. (S10) gives $\mathcal{C} \approx 1$, and then Eq. (S11) recovers the arcsin law Eq. (2). Expanding Eq. (S10) to the next order of $1/t_w$, we obtain,

$$\begin{aligned} \mathcal{C} &= 1 - \frac{\sin(\pi x)}{\pi\Gamma(x)} \int_0^{\infty} du (1+u)^{-1} u^{-x} \Gamma \left(x, \frac{u}{1+u} \frac{t_w}{\tau_0} \right) \\ &\approx 1 - \frac{1}{(1-x)\Gamma(1-x)\Gamma^2(x)} \left(\frac{t_w}{\tau_0} \right)^{x-1}. \end{aligned} \quad (\text{S12})$$

Combining Eqs. (S11), (S12) and (2) gives,

$$\begin{aligned}\Pi_w^{\text{BTM}}(t_w) &\approx H(w, x) \left[1 + \frac{1}{(1-x)\Gamma(1-x)\Gamma^2(x)} \left(\frac{t_w}{\tau_0} \right)^{x-1} \right] \\ &= H(w, x) \left[1 + A \left(\frac{t_w}{\tau_0} \right)^{-\alpha} \right],\end{aligned}\quad (\text{S13})$$

where $\alpha = 1 - x$ and $A = \frac{1}{(1-x)\Gamma(1-x)\Gamma^2(x)}$. We have thus derived the large- t_w form of Eq. (5). Finally, we compare the analytic expression Eq. (S13) with the numerical results obtained by the inverse Laplace transform of the exact expressions Eqs. (S5) and (S6), confirming the validity of Eq. (S13) in the asymptotic regime (see Fig. S2a). Note that, without loss of generality, we fix $w = 0.5$ in this study.

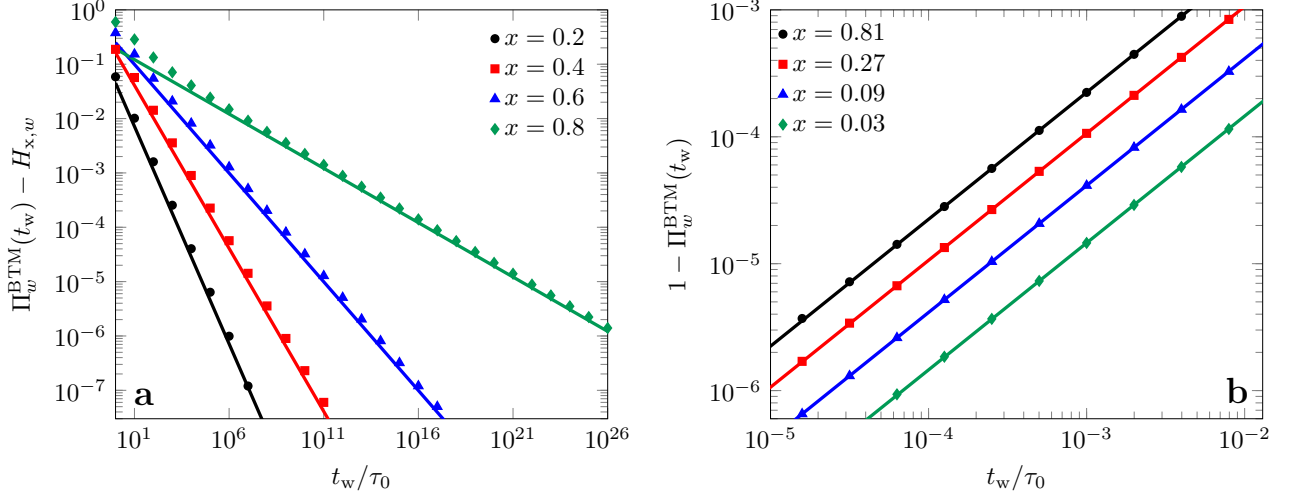


FIG. S2. Comparison between the analytical approximation of the aging function for the BTM and the exact numerical results using the inverse Laplace transform. (a) Large- t_w power-law convergence to the asymptotic plateau. (b) Small- t_w linear decay. The points are exact results obtained by the numerical inverse Laplace transform of Eqs. (S5) and (S6). The solid lines are Eq. (S13) in (a) and Eq. (S18) in (b).

C. Short-time linear decay

For short-time dynamics, similarly we begin with Eq. (S6) in the last section. In the short-time limit $t_w \rightarrow 0$ (corresponding to the limit $s \rightarrow \infty$), ${}_2F_1(1, x; 1 + x; -\frac{1}{s\tau_0}) \approx 1$, and

$$\hat{Q}(s, \tau) \approx \frac{1}{\mathcal{C}N_b} \frac{s\tau}{s\tau + 1}. \quad (\text{S14})$$

The probability distribution $Q(t_w, \tau)$ is again obtained by the inverse Laplace transform:

$$Q(t_w, \tau) = \frac{1}{\mathcal{C}N_b} e^{-t_w/\tau}. \quad (\text{S15})$$

Then the aging function is obtained,

$$\begin{aligned}\Pi(t_w, t_w + t) &= N_b \int_{\tau_0}^{\infty} d\tau Q(t_w, \tau) e^{-t/\tau} \psi(\tau) \\ &= \frac{x}{\mathcal{C}} \left(\frac{t + t_w}{\tau_0} \right)^{-x} \left[\Gamma(x) - \Gamma \left(x, \frac{t + t_w}{\tau_0} \right) \right] \\ &= \left(\frac{t_w}{t + t_w} \right)^x \frac{\Gamma(x) - \Gamma \left(x, \frac{t + t_w}{\tau_0} \right)}{\Gamma(x) - \Gamma \left(x, \frac{t_w}{\tau_0} \right)},\end{aligned}\quad (\text{S16})$$

where the normalized constant is,

$$\begin{aligned} \mathcal{C} &= \int_{\tau_0}^{\infty} d\tau e^{-t_w/\tau} \psi(\tau) \\ &= x \left(\frac{t_w}{\tau_0} \right)^{-x} \left[\Gamma(x) - \Gamma \left(x, \frac{t_w}{\tau_0} \right) \right]. \end{aligned} \quad (\text{S17})$$

Expanding Eq. (S16) around $t_w = 0$, we obtain,

$$\Pi_w^s(t_w) \approx 1 - \frac{wx}{x+1} \left(\frac{t_w}{\tau_0} \right) = 1 - C \left(\frac{t_w}{\tau_0} \right). \quad (\text{S18})$$

Similar to the long-time case, the analytic result Eq. (S18) can be confirmed by exact numerical calculations using the inverse Laplace transform (see Fig. S2b).

D. Logarithmic decay due to finite-size effects in the generalized trap model

The GTM aging function is computed using the formula Eq. (S1),

$$\begin{aligned} \Pi_w^{\text{GTM}}(t_w) &= \int_{\tau_0}^{\infty} d\tau \psi_{\text{GTM}}(\tau) Q_{\text{GTM}}(t_w, \tau) e^{-wt_w/\tau} \\ &= \int_0^{\infty} d\tau e^{f_{\text{GTM}}(t_w, \ln \tau)}. \end{aligned} \quad (\text{S19})$$

The GTM barrier energy distribution Eq. (3) leads to the modified trapping time distribution (via the Arrhenius law),

$$\begin{aligned} \psi_{\text{GTM}}(\tau) &\sim \tau^{-\hat{x}-1} \exp[-\mu \ln^2(\tau/\tau_0)] \\ &\sim \tau^{-\hat{x}-\mu \ln(\tau/\tau_0)-1}, \end{aligned} \quad (\text{S20})$$

where $\mu \equiv \frac{T^2}{2Na}$, and $\hat{x} = \left(1 - \frac{\bar{E}T_c}{Na}\right)x$. The $Q_{\text{GTM}}(t_w, \tau)$ can be computed by the inverse Laplace transform of Eq. (S5), where $\left\langle \frac{s\tau}{s\tau+1} \right\rangle = \int_{\tau_0}^{\infty} d\tau \frac{s\tau}{s\tau+1} \psi_{\text{GTM}}(\tau)$.

It is hard to directly analyze Eq. (S19). However, based on a saddle-point approximation, we find that the aging functions in the two models can be related by shifting the effective reduced temperature,

$$\Pi_w^{\text{GTM}}(t_w; x) \sim \Pi_w^{\text{BTM}}(t_w; \tilde{x}), \quad (\text{S21})$$

where

$$\tilde{x} = \left(1 - \frac{\bar{E}T_c}{Na}\right)x + \frac{T^2}{Na} \ln t_w = \hat{x} + 2\mu \ln t_w. \quad (\text{S22})$$

In other words, the aging function $\Pi_w^{\text{GTM}}(t_w; x)$ of the GTM at a temperature $T = T_c x$ is approximately equivalent to the aging function $\Pi_w^{\text{BTM}}(t_w; \tilde{x})$ of the BTM at the temperature $T = T_c \tilde{x}$ with \tilde{x} given by Eq. (S22). Equation (S21) is essentially due to the relation between the maximum of $f_{\text{GTM}}(t_w, \ln \tau)$ in Eq. (S19) and that of $f_{\text{BTM}}(t_w, \ln \tau)$,

$$\ln \tau_{\text{GTM}}^*(t_w, x) \approx \ln \tau_{\text{BTM}}^*(t_w, \tilde{x}), \quad (\text{S23})$$

where $f(t_w, \ln \tau)$ is maximized at $\ln \tau^*$ with other parameters (t_w , T , etc.) fixed. Equation (S23) is consistent with the numerically evaluated maximum point $\ln \tau^*$ (see Fig. S3). As shown by the data, in general $\ln \tau^* \sim \ln t_w$ in both models (Fig. S3a,b). The GTM data at x and the BTM data at the corresponding \tilde{x} (see Eq. S22) collapse for different x and N (Fig. S3c,d), and thus Eq. (S23) is verified.

Equation (S22) means that, the Gaussian term in the GTM barrier distribution Eq. (3) gives rise to two effects compared to the BTM. First, it shifts the reduced temperature effectively from $x = T/T_c$ to an N -independent \hat{x} . This shift modifies the asymptotic plateau of the aging function from $H(w, x)$ to $H(w, \hat{x})$, in the thermodynamic limit $N \rightarrow \infty$. Second, the next-order correction adds a term $\frac{1}{N} \ln t_w$ as $\tilde{x} - \hat{x} \sim \frac{1}{N} \ln t_w$. This correction disappears in the thermodynamic limit, but brings in a $\ln(t_w)$ decay term to the aging function for a finite N , as we show below.

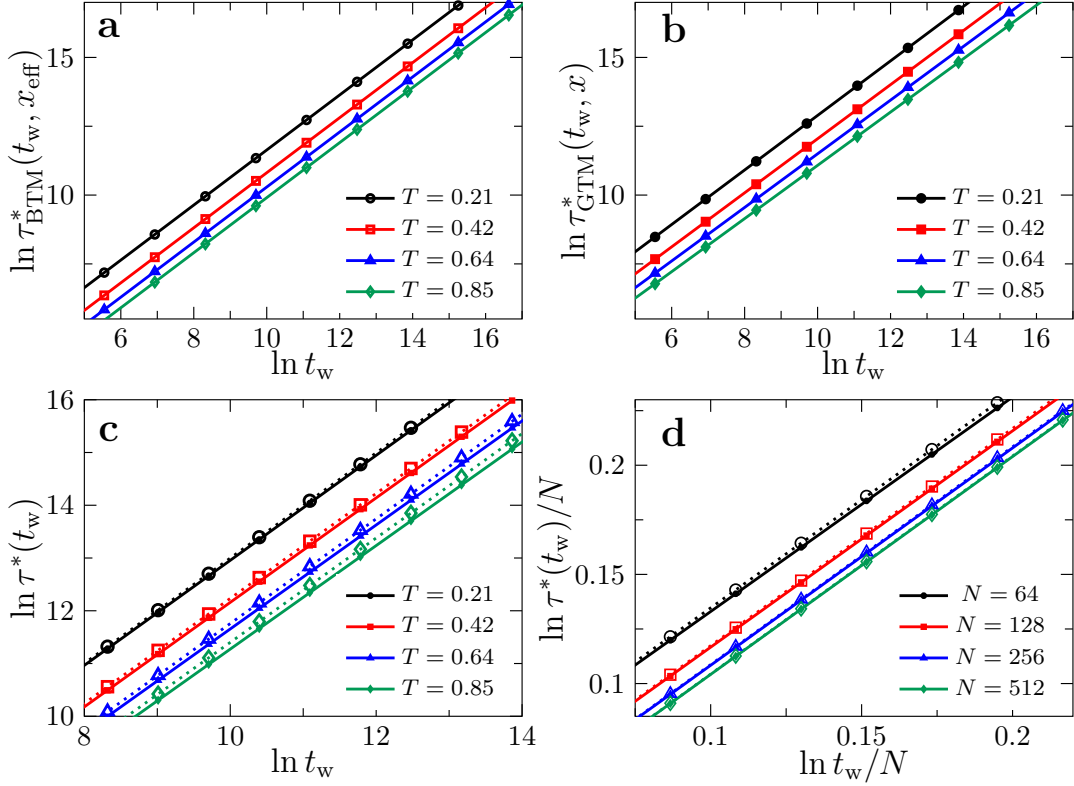


FIG. S3. Verification of Eq. (S23). The data points are obtained by numerical evaluation of the maximum $f(t_w, \ln \tau^*)$ of the function $f(t_w, \ln \tau)$ defined in Eq. (S19). As shown by the data, $\ln \tau^*$ is linearly proportional to $\ln t_w$ in (a) BTM and (b) GTM, for $T = 0.21, 0.42, 0.64, 0.85$ (or $x = 0.25, 0.5, 0.75, 1.0$), and $N = 64$. At the same T , the BTM and GTM data do not collapse in (a,b). However, the GTM data (dotted point-line) at $T = T_c x$ and the BTM data (solid point-line) at $T = T_c \tilde{x}$ collapse, where \tilde{x} is given by Eq. (S22), for different (c) T (with $N = 128$ fixed) and (d) N (with $T = 0.42$ fixed).

With Eq. (S21), $\Pi_w^{\text{GTM}}(t_w)$ can be conveniently analyzed using the arcsin law, with x in Eq. (S13) replaced by \tilde{x} . For large N , the difference between \tilde{x} and \hat{x} , $\tilde{x} - \hat{x} \sim \frac{1}{N} \ln t_w$, can be considered as a perturbation to the original form. Expanding around \hat{x} to the first order, we obtain,

$$\begin{aligned}
 \Pi_w^{\text{GTM}}(t_w) &\approx H(w, \tilde{x}) \left[1 + A \left(\frac{t_w}{\tau_0} \right)^{-\alpha} \right] \\
 &\approx H(w, \hat{x}) \left[1 + A \left(\frac{t_w}{\tau_0} \right)^{-\alpha} \right] + \frac{T^2}{Na} \frac{\partial H(w, \hat{x})}{\partial \hat{x}} \ln \left(\frac{t_w}{\tau_0} \right) \\
 &= H(w, \hat{x}) \left[1 + A \left(\frac{t_w}{\tau_0} \right)^{-\alpha} \right] - \frac{B}{N} \ln \left(\frac{t_w}{\tau_0} \right),
 \end{aligned} \tag{S24}$$

where $B = -\frac{T^2}{a} \frac{\partial H(w, \hat{x})}{\partial \hat{x}}$. The analytic expression of the logarithmic decay $-\frac{B}{N} \ln \left(\frac{t_w}{\tau_0} \right)$ with $B = -\frac{T^2}{a} \frac{\partial H(w, \hat{x})}{\partial \hat{x}}$ is compared to the numerical integration of Eq. (S19) in Fig. S4: the agreement is converged with increasing N . We further compare the theoretical results $-\frac{B}{N} \ln \left(\frac{t_w}{\tau_0} \right)$ with the MC data in Fig. S5. While the logarithmic form is robust, the coefficient B is not exact due to strong higher-order corrections for small N in MC simulations. In the main text Fig. 3d, we treat B as a fitting parameter.

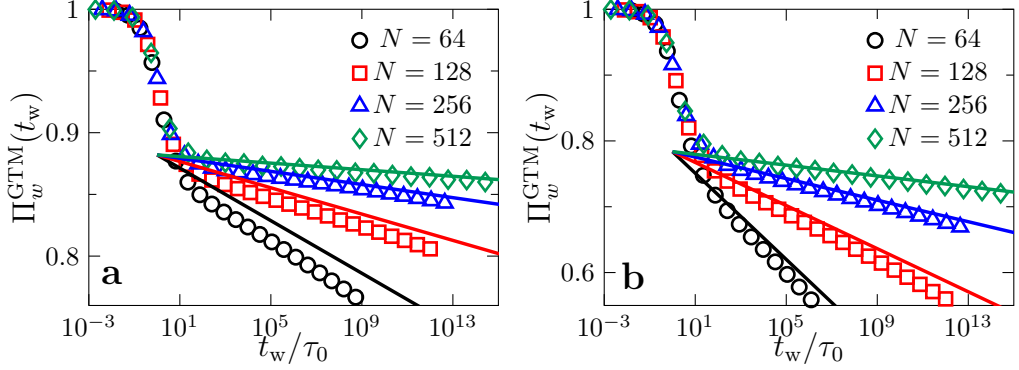


FIG. S4. Logarithmic decay in the GTM at (a) $T = 0.64$ and (b) $T = 1$. The data points are obtained by numerical integration of Eq. (S19). The lines are the $-\frac{B}{N} \ln\left(\frac{t_w}{\tau_0}\right)$ term in Eq. (S24).

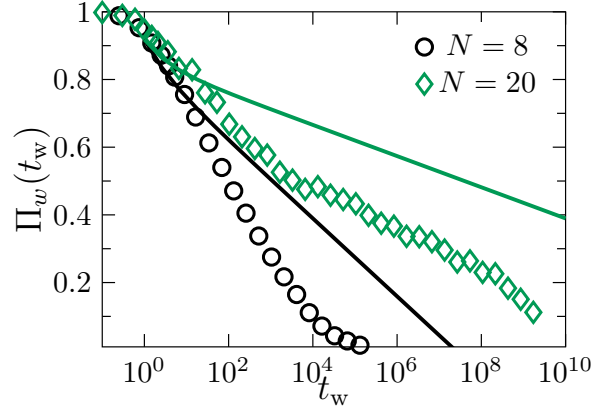


FIG. S5. Comparison between the MC aging function (points) and Eq. (S24) (lines), at $T = 0.75$. No fitting parameters are used for the lines.

S2. ADDITIONAL SIMULATION DATA FOR THE RANDOM ENERGY MODEL

A. Energy trajectory

We show an example of the time trajectory of the configuration energy $E(t_w)$ for the G-REM (Fig. S6a), and the corresponding trajectory of the basin (saddle point) energy $\tilde{E}(t_w)$ (Fig. S7b).

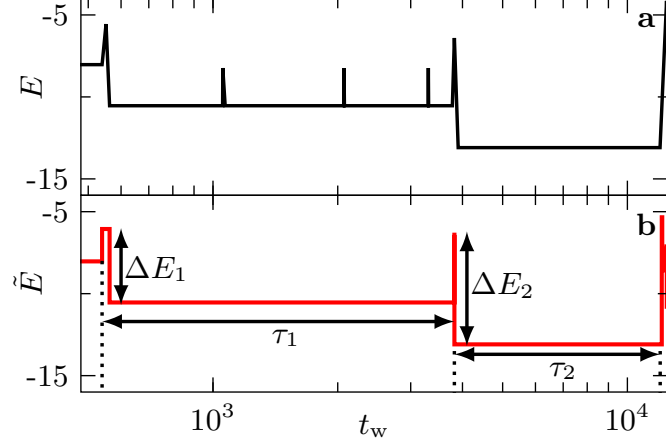


FIG. S6. An energy trajectory obtained by the MC simulation of the G-REM. Data are obtained at $T = 0.75$ with $N = 20$. (a) An example of configuration trajectory, where $E(t_w)$ is the energy of the configuration at t_w . (b) Corresponding basin trajectory, where $\tilde{E}(t_w)$ is the energy of the basin or the saddle point at t_w . With this, a sequence of hopping events with the barrier energy ΔE_{i_k} and the hopping time τ_k are identified.

B. Test of the renewal mechanism

Occasionally, after leaving a basin, the system jumps back to the same basin. Following the previous study [38], the two events are merged in such cases. The effects of return jumps are revealed in Fig. S7(a,b) by the conditional probability $p(\tau_2|\tau_1)$, which is the distribution of the next-event hopping time τ_2 when the current-event hopping time is τ_1 . Only when the return jumps are merged, the $p(\tau_2|\tau_1)$ is independent of τ_1 , which means that the two consecutive jumps are independent. The independence of consecutive jumps (the renewal mechanism) is a basic assumption in the trap model. In order to be consistent with the renewal mechanism, we employ the no-return treatment.

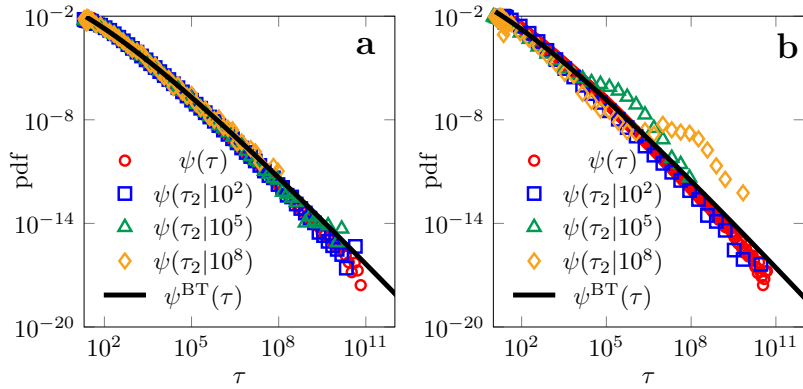


FIG. S7. Test of the renewal mechanism in the G-REM. Data are obtained by MC simulations at $T = 0.75$ with $N = 20$. (a) The hopping time probability distribution function (pdf) $\psi(\tau)$ and the conditional distribution $\psi(\tau_2|\tau_1)$ measured in MC simulations, (b) without and (d) with return hops; $\psi^{BT}(\tau)$ is converted from the static distribution $p_{G-REM}^{BT}(\Delta E)$ using the Arrhenius law.

C. Verification of the Arrhenius law

In the trap model, the hopping time τ and the barrier energy ΔE are related through the Arrhenius law,

$$\tau(\Delta E) = A_0 \exp(\Delta E/T). \quad (\text{S25})$$

We find that the Arrhenius law is consistent with the $\bar{\tau}(\Delta E)$ data ($\bar{\tau}$ is the mean hopping time for the given ΔE) obtained by MC simulations (Fig. S8a), with $A_0 \sim O(1)$ as shown in Fig. S8b-inset (the time unit is N).

When N is finite, for a given ΔE , τ follows a distribution

$$\Psi(\tau|\Delta E) = (1 - \eta)^{\tau-1} \eta \approx e^{-\tau\eta} \eta, \quad (\text{S26})$$

where $\eta = \exp(-\Delta E/T)$. To derive $\Psi(\tau|\Delta E)$, consider a discretized time τ : if a system is trapped in a basin with a ΔE -barrier for τ steps, it should remain in the basin for $\tau - 1$ steps with a probability $1 - \eta$ at each step, and jumps out the basin at the final step with a probability η . Equation (S26) is also verified by the simulation data (see Fig. S8b). Note that the mean hopping time of Eq. (S26), $\bar{\tau}(\Delta E) = \int_0^\infty \tau \Psi(\tau|\Delta E) d\tau$, consistently recovers the Arrhenius law Eq. (S25). In short, the Arrhenius law is verified by our MC data.

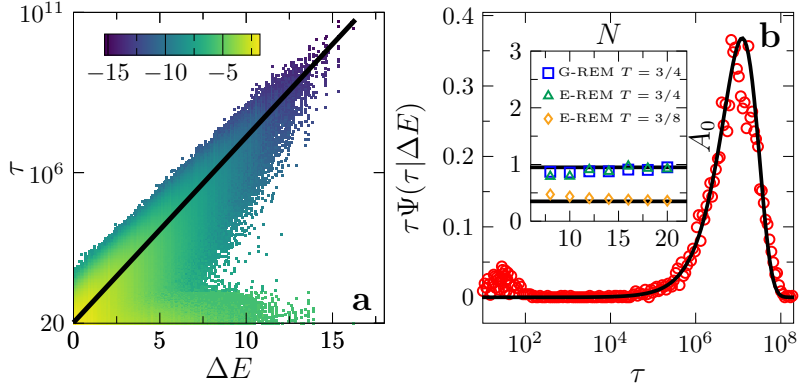


FIG. S8. Arrhenius law. (a) Correspondence between τ and ΔE in MC simulations of the G-REM at $T = 0.75$ with $N = 20$, where the color represents the logarithm of the joint probability $\ln \Psi(\tau, \Delta E)$ (see the color bar). (b) The conditional probability $\Psi(\tau|\Delta E = 10)$ multiplied by τ ; the solid line follows Eq. (S26). (b-inset) A_0 vs N .

S3. THERMODYNAMICS OF THE FINITE-SIZE RANDOM ENERGY MODEL: A TREE-EXPANSION THEORY

A. Probability distributions

Our aim is to obtain statistical properties of the energy landscape for the finite-sized REM with N spins, where N is sufficiently small so that the system is far from the thermodynamic limit ($N \rightarrow \infty$). We assume that each basin only has one nondegenerate local minimum, and that basins are independent. The probability distribution of the local minimum E_{lm} is,

$$\begin{aligned} p_N^{\text{lm}}(E_{\text{lm}}) &= (N+1)\rho(E_{\text{lm}}) \left[\int_{E_{\text{lm}}}^{\infty} dE \rho(E) \right]^N \\ &= (N+1)\rho(E_{\text{lm}}) L^N(E_{\text{lm}}), \end{aligned} \quad (\text{S27})$$

where $L(E) \equiv \int_E^{\infty} dE \rho(E)$ is a complementary cumulative distribution function, and $\rho(E)$ is the probability distribution function of the configuration energy E . The above expression requires that the N direct neighbors of the local minimum, which are related to the local minimum by a single spin flip, have an energy E higher than E_{lm} . The factor $N+1$ comes from the $N+1$ choices of the local minimum among the $N+1$ configurations. For the G-REM, $\rho(E) = \rho_{\text{Gauss}}(E)$ given by Eq. (7), which results in $L(E) = L_{\text{Gauss}}(E)$, where

$$L_{\text{Gauss}}(E) = \frac{1}{2} \text{erfc}(E/\sqrt{2N}), \quad (\text{S28})$$

with $\text{erfc}(x)$ the complementary error function. For the E-REM, $\rho(E) = \rho_{\text{exp}}(E)$ as in Eq. (8), and $L(E) = L_{\text{exp}}(E)$, where

$$L_{\text{exp}}(E) = [1 - \exp(E)]\Theta(-E). \quad (\text{S29})$$

The probability distributions of the saddle point energy E_{sp} and the barrier energy ΔE cannot be explicitly obtained. They need to be computed by integrating out the other variable in the joint distribution $\lambda_N(E_{\text{lm}}, E_{\text{sp}})$,

$$p_N^{\text{sp}}(E_{\text{sp}}) = \int_{-\infty}^{+\infty} dE_{\text{lm}} \lambda_N(E_{\text{lm}}, E_{\text{sp}}), \quad (\text{S30})$$

$$p_N(\Delta E) = \int_{-\infty}^{+\infty} dE_{\text{sp}} \lambda_N(E_{\text{sp}} - \Delta E, E_{\text{sp}}). \quad (\text{S31})$$

The joint distribution $\lambda_N(E_{\text{lm}}, E_{\text{sp}})$ characterizes the probability of a basin with a local minimum energy E_{lm} and a saddle point energy E_{sp} . Our key task is to compute $\lambda_N(E_{\text{lm}}, E_{\text{sp}})$. To do that, we develop an approach named *tree-expansion theory*. The starting point is to write $\lambda_N(E_{\text{lm}}, E_{\text{sp}})$ as a summation,

$$\lambda_N(E_{\text{lm}}, E_{\text{sp}}) \equiv \sum_{\Omega=1}^N \lambda_N^{(\Omega)}(E_{\text{lm}}, E_{\text{sp}}), \quad (\text{S32})$$

where Ω is the number of configurations in the basin. For example, $\Omega = 1$ means that there is only a local minimum in the basin, and $\Omega = 2$ means that there is another configuration in the basin besides the local minimum, etc. The summation converges quickly with the increasing Ω . We next explicitly consider the first three orders, $\Omega = 1, 2, 3$.

1. The first order: $\Omega = 1$

When $\Omega = 1$, as shown in Fig. S9, the basin contains only the local minimum without any other configurations. By definition, the saddle point should have the lowest energy among the N neighbors of the local minimum – the probability of this condition is $L^{N-1}(E_{\text{sp}})$. The saddle point also has N neighbors, including the local minimum and $N-1$ other neighbors. The energies of the other $N-1$ neighbors cannot be all higher than E_{sp} – otherwise the saddle point would be a configuration inside the basin (not a saddle point). This condition imposes a constraint given by $1 - L^{N-1}(E_{\text{sp}})$. Putting these considerations together, we can write the first-order joint distribution as

$$\lambda_N^{(1)}(E_{\text{lm}}, E_{\text{sp}}) = (N+1)N\rho(E_{\text{lm}})\rho(E_{\text{sp}})L^{N-1}(E_{\text{sp}}) [1 - L^{N-1}(E_{\text{sp}})], \quad (\text{S33})$$

where the extra factor $(N+1)N$ comes from the permutation of choosing a local minimum from the $N+1$ configurations and a saddle point from the rest of the N configurations.

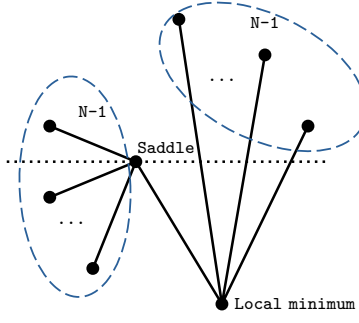


FIG. S9. Graphic representation of the first-order joint distribution Eq. (S33). Each node represents a configuration, and the height of the node represents the configuration energy E . Any pair of configurations connected by a link are related by a single-spin flip. The saddle point energy E_{sp} is marked by the dotted line. For $\Omega = 1$, there is only one configuration in the basin ($E < E_{\text{sp}}$), which is the local minimum. The number of nodes in the circled cluster is indicated (in this case, both clusters have $N - 1$ nodes). For simplification, only $N = 4$ are shown.

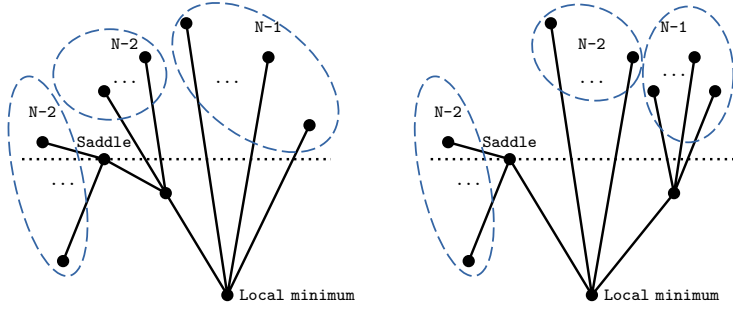


FIG. S10. Graphic representation of the second-order joint distribution Eq. (S34).

2. The second order: $\Omega = 2$

The second-order joint distribution corresponds to two graphs as shown in Fig. S10. Besides the local minimum, the basin contains one configuration whose energy is between E_{sp} and E_{lm} – the corresponding probability is $\int_{E_{\text{lm}}}^{E_{\text{sp}}} dE \rho(E)$. The permutation of choosing one saddle point, one local minimum and another configuration in the basin gives a factor of $(N + 1)N(N - 1)$. The two graphs in Fig. S10 coincidentally have the same expression, which gives an extra factor of two. Finally, the second-order joint distribution can be written as,

$$\begin{aligned} \lambda_N^{(2)}(E_{\text{lm}}, E_{\text{sp}}) &= 2(N + 1)N(N - 1)\rho(E_{\text{lm}})\rho(E_{\text{sp}})L^{2N-3}(E_{\text{sp}}) [1 - L^{N-2}(E_{\text{sp}})] \int_{E_{\text{lm}}}^{E_{\text{sp}}} dE \rho(E) \\ &= 2(N + 1)N(N - 1)\rho(E_{\text{lm}})\rho(E_{\text{sp}})L^{2N-3}(E_{\text{sp}}) [1 - L^{N-2}(E_{\text{sp}})] [L(E_{\text{lm}}) - L(E_{\text{sp}})] \end{aligned} \quad (\text{S34})$$

3. The third order: $\Omega = 3$

To compute the third-order joint distribution, we need to consider six graphs as shown in Fig. S11. The top three graphs correspond to the term with $1 - L^{N-3}(E_{\text{sp}})$ in the following expression Eq. (S35), and the bottom three graphs correspond to the term with $1 - L^{N-2}(E_{\text{sp}})$:

$$\begin{aligned} \lambda_N^{(3)}(E_{\text{lm}}, E_{\text{sp}}) &= 3(N + 1)N(N - 1)\rho(E_{\text{lm}})\rho(E_{\text{sp}})L^{3N-6}(E_{\text{sp}}) \times \\ &\quad \times \{(N - 2) [1 - L^{N-3}(E_{\text{sp}})] + (N - 1) [1 - L^{N-2}(E_{\text{sp}})]\} \int_{E_{\text{sp}} > E_1 > E_2 > E_{\text{lm}}} dE_1 dE_2 \rho(E_1)\rho(E_2) \\ &= \frac{3}{2}(N + 1)N(N - 1)\rho(E_{\text{lm}})\rho(E_{\text{sp}})L^{3N-6}(E_{\text{sp}}) \times \\ &\quad \times \{(N - 2) [1 - L^{N-3}(E_{\text{sp}})] + (N - 1) [1 - L^{N-2}(E_{\text{sp}})]\} [L(E_{\text{lm}}) - L(E_{\text{sp}})]^2. \end{aligned} \quad (\text{S35})$$

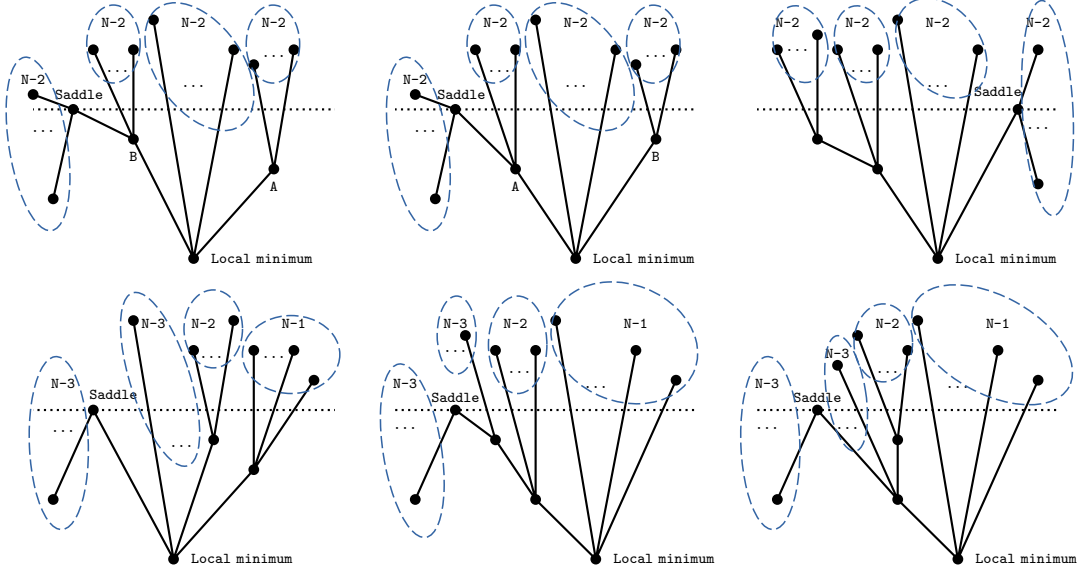


FIG. S11. Graphic representation of the third-order joint distribution Eq. (S35).

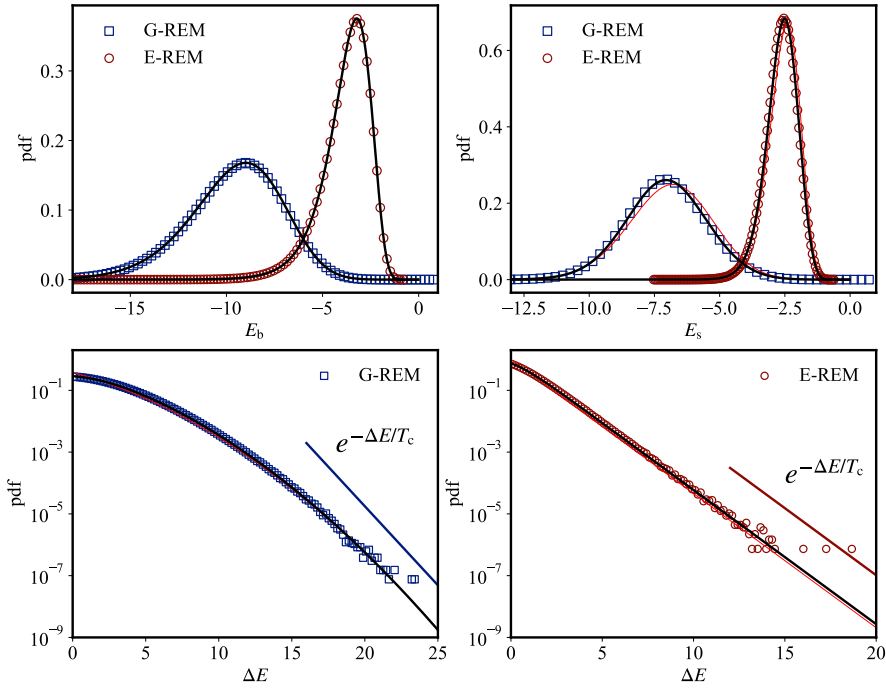


FIG. S12. Comparison between the tree-expansion theory (lines) and the barrier-tree method (points), for the G-REM and E-REM with $N = 24$ spins. (a) Probability distribution function (pdf) of the local minimum energy. The line represents Eq. (S27). (b) Pdf of the saddle point energy. (c,d) Pdf of the barrier energy distribution. In (b-d), the red line represents the tree-expansion theoretical results up to the first-order ($\Omega = 1$), and the black line represents the results up to the third-order results ($\Omega = 3$).

4. Verification with the numerical barrier-tree algorithm

The above theoretical results are compared with the numerical data obtained by the barrier-tree algorithm for both G-REM and E-REM with $N = 24$ spins (Fig. S12). The expression Eq. (S27) of the local minimum energy distribution $p_N^{\text{lm}}(E_{\text{lm}})$ is tested in Fig. S12a. The tree-expansion results of the saddle point energy distribution $p_N^{\text{sp}}(E_{\text{sp}})$ (see Eq. S30) and the barrier energy distribution $p_N(\Delta E)$ (see Eq. S31) are tested in Fig. S12b-d. It can be seen that the first-order results are already very close to the numerical data. Note that the distribution $\rho(E)$ in the theoretical expressions shall be replaced by Eqs. (7) and (8) in the Appendix for the corresponding REMs.

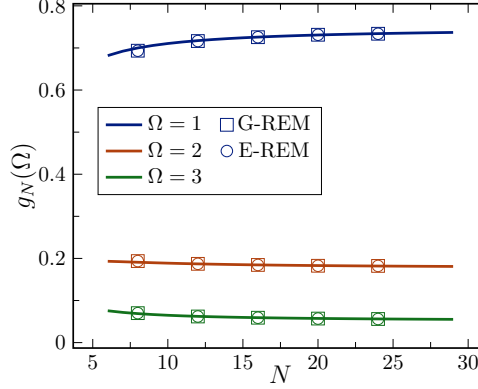


FIG. S13. Probability $g_N(\Omega)$ of having Ω configurations in a basin. Lines are tree-expansion theory results Eq. (S37), and points are numerical data obtained by the barrier-tree algorithm.

B. Internal entropy

The probability of having Ω configurations in a basin is,

$$g_N(\Omega) = \int_{-\infty}^{\infty} dE_{\text{sp}} \int_{-\infty}^{E_{\text{sp}}} dE_{\text{lm}} \lambda_N^{(\Omega)}(E_{\text{lm}}, E_{\text{sp}}). \quad (\text{S36})$$

Using the above tree-expansion results, Eqs. (S33), (S34) and (S35), we obtain the first three orders,

$$\begin{aligned} g_N(1) &= \int_{-\infty}^{\infty} dE_{\text{sp}} \rho(E_{\text{sp}}) N(N+1) L^{N-1}(E_{\text{sp}}) [1 - L^{N-1}(E_{\text{sp}})] [1 - L(E_{\text{sp}})] \\ &= \int_0^1 d\sigma N(N+1) \sigma^{N-1} (1 - \sigma^{N-1}) (1 - \sigma) \\ &= \frac{3N-3}{4N-2} \\ &\xrightarrow{N \rightarrow \infty} \frac{3}{4}, \\ g_N(2) &= \int_0^1 d\sigma (N-1) N(N+1) \sigma^{2N-3} (1 - \sigma^{N-2}) (1 - \sigma)^2 \\ &= \frac{(N+1)(N-2)(19N-12)}{6(2N-1)(3N-4)(3N-2)} \\ &\xrightarrow{N \rightarrow \infty} \frac{19}{108}, \\ g_N(3) &= \int_0^1 d\sigma (N-1) N(N+1) \sigma^{3N-6} \left[\frac{N-2}{2} (1 - \sigma^{N-3}) + \frac{N-1}{2} (1 - \sigma^{N-2}) \right] (1 - \sigma)^3, \\ &= \frac{N(N+1)(2N-3)}{(3N-5)(3N-4)(3N-2)} - \frac{3(N-1)N(N+1)}{4(2N-3)(4N-7)(4N-5)} \\ &\xrightarrow{N \rightarrow \infty} \frac{175}{3456}. \end{aligned} \quad (\text{S37})$$

Note that the results in Eq. (S37) are model-independent, i.e., independent of $\rho(E)$. The numerical data obtained by the barrier-tree algorithm confirm the tree-expansion theory Eq. (S37) (see Fig. S13).

In the thermodynamic limit ($N \rightarrow \infty$), the probability $g_N(\Omega)$ converges to an analytical expression that is universal for any Ω ,

$$\begin{aligned} g_\infty(\Omega) &= \lim_{N \rightarrow \infty} \int_0^1 d\sigma \frac{N!}{(N - \Omega - 1)!} \sigma^{\Omega N - \frac{1}{2}\Omega(\Omega+1)} (1 - \sigma^{N-\Omega}) (1 - \sigma)^\Omega \\ &= \lim_{N \rightarrow \infty} \frac{N! \Omega!}{(N - \Omega - 1)!} \left[\frac{(\Omega N - \frac{1}{2}\Omega(\Omega+1))!}{(\Omega N - \frac{1}{2}\Omega(\Omega+1) + 1)!} - \frac{((\Omega+1)N - \frac{1}{2}\Omega(\Omega+3))!}{((\Omega+1)N - \frac{1}{2}\Omega(\Omega+1) + 1)!} \right] \\ &= \frac{\Omega!}{\Omega^{\Omega+1}} - \frac{\Omega!}{(\Omega+1)^{\Omega+1}}. \end{aligned} \quad (\text{S38})$$

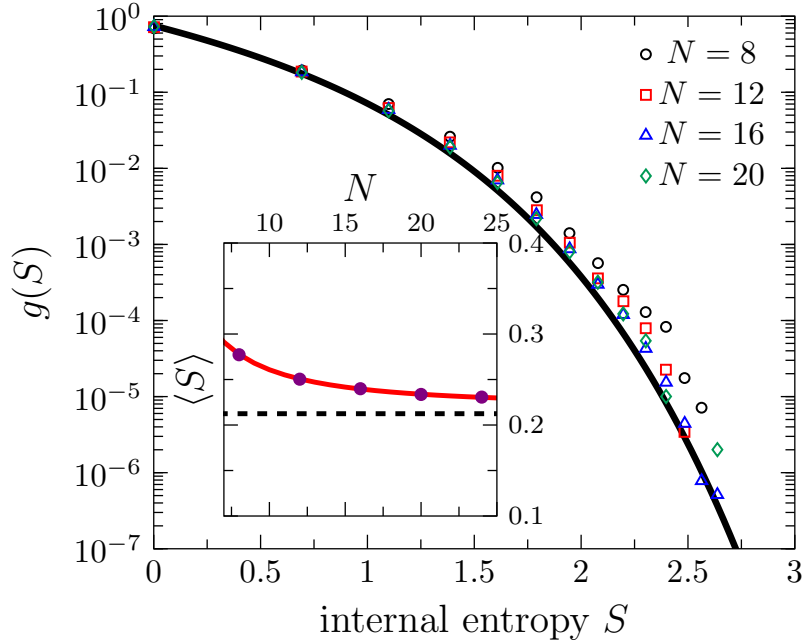


FIG. S14. Probability distribution function of the internal entropy for the G-REM. The data points are $g^{\text{BT}}(S)$ obtained by the numerical barrier-tree method, and the solid line is Eq. (S38). (inset) Average numerical entropy $\langle S \rangle$ as a function of N , where the dashed line is $S_\infty \approx 0.212439$ (Eq. S39).

The internal entropy of the whole system in the thermodynamic limit is

$$S_\infty \equiv \sum_{\Omega=1}^{\infty} g_\infty(\Omega) \log \Omega \approx 0.212439. \quad (\text{S39})$$

This result is consistent with the numerical data obtained by the barrier-tree method (see Fig. S14). The inset of Fig. S14 shows that the mean internal entropy $\langle S \rangle$ converges to a value $S_\infty \approx 0.21$ in the large- N limit. Then the average number of configurations in a basin is $\Omega \approx e^{0.21} \approx 1.2$, i.e., each basin contains approximately one configuration in average. Thus in the spin glass phase, the mean internal entropy per spin vanishes ($\langle S \rangle/N \rightarrow 0$) in the thermodynamic limit, consistent with thermodynamic theory of the REM [33].

C. Number of basins

We assume that each basin contains one local minimum. Two local minima cannot be directly related via a single-spin flip – otherwise the two basins cannot be separated. Thus, in average, we can assume that each basin occupies $N + 1$ configurations, i.e., one local minimum and its N neighbours. The total number of configurations for a N -spin

REM is 2^N . Therefore, the total number of basins is,

$$N_b = \frac{2^N}{N+1}. \quad (\text{S40})$$

Figure **S15** shows that this simple consideration Eq. (S40) describes well the numerical data obtained by the barrier-tree method.

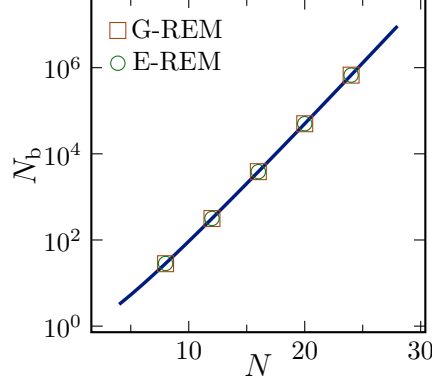


FIG. S15. Number of basins N_b as a function of the system size N . The line represents Eq. (S40), and the points are data obtained by the numerical barrier-tree algorithm.

S4. ADDITIONAL SIMULATION DATA FOR STRUCTURAL GLASSES

A. Comparison of different simulation algorithms for the WCA model.

We have checked that the aging functions $F_w(t_w)$ obtained by different simulation methods are consistent with each other, apart from the short-time dynamics that are protocol-dependent (see Fig. S16a). Four different simulation methods are compared. (i) MD simulations in the isokinetic ensemble. (ii) MD simulations in the microcanonical (NVE) ensemble with the kinetic energy rescaled to the target value every 50 MD steps (0.1 LJ time units). (iii) MD simulations in the canonical (NVT) ensemble using the Nose-Hoover chain thermostat with a damping parameter of 0.1 LJ time units [85]. (iv) Standard MC simulations in the canonical ensemble. In the MC simulation, we attempt to translate a particle by a displacement vector randomly drawn in a sphere of a radius $5 \times 10^{-2} \sigma_{\text{AA}}$. The move is accepted according to the Metropolis acceptance rule. In Fig. S16, the MC steps are multiplied by 6.0×10^{-4} to match the long-time dynamics with those obtained by MD simulations. Further comparison is carried out for the non-equilibrium two-time mean-squared displacement (MSD), $\delta r^2(t_w, t_w + t) \equiv \frac{1}{N_A} \langle \sum_{i=1}^{N_A} |\mathbf{r}_i(t_w + t) - \mathbf{r}_i(t_w)|^2 \rangle$ (see Fig. S16b). These tests validate the isokinetic ensemble adapted in our MD simulations, which is used to generate the results reported in the current study.

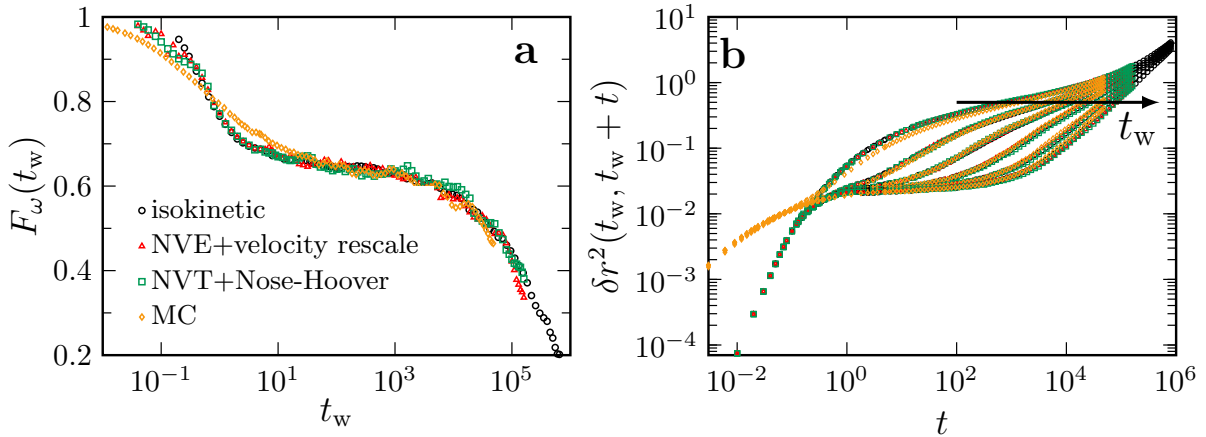


FIG. S16. Comparison of the results obtained by different MD and MC algorithms for the WCA model. (a) Aging function $F_w(t_w)$ and (b) non-equilibrium two-time MSD $\delta r^2(t_w, t_w + t)$ for $N = 1000$ particles at $T = 0.25$. In panel (b), $t_w \approx 1.0, 16.0, 135, 1.15 \times 10^3, 9.65 \times 10^3, 4.21 \times 10^4$ from left to right.

B. Absence of crystallization and phase separation during aging in the WCA model.

The growth of crystals is marked by the emergence of Bragg peaks in the measured structure factor, $S(q)$, which are absent in the liquid state [89]. Therefore, a constant $S(q)$ is a standard criterion for ruling out crystallization in amorphous systems [50]. During aging of the WCA system, we observe negligible change in $S(q)$ for both total and partial static structure factor (Fig. S17a-b), which suggests that crystallization is not occurring. This finding is consistent with the fact that the nucleation time, τ_X , typically exceeds the α -relaxation time, τ_{eq} , by orders of magnitude [90]; since aging takes place prior to equilibration, crystallization is not expected on this timescale.

A more sensitive probe of long-range order is $S_0 = S(q \rightarrow 0)$, obtained by extrapolating the short-wavelength behavior of $S(q)$ (Fig. S17a-b, inset). Within the Ornstein-Zernike theory, S_0 is proportional to the square of the correlation length, ξ_{OZ}^2 , which characterizes positional pair correlations [91]. Our data show that S_0 initially decreases weakly with waiting time, t_w , during aging (Fig. S17c-d). Only after $t_w \approx 10^5$, does S_0 begin to increase. This late-stage growth implies the development of long-range order, possibly due to subtle fractionation or phase separation. However, these effects are minimal, as evidenced by the similar behavior of the full $S(q)$ and the partial $S^{AA}(q)$ for large (type A) particles. Moreover, the finite-size effects are insignificant.

Crucially, these potential fractionation effects manifest at t_w values far beyond the aging regime central to this study. This is clear from two observations. First, the aging relation $\tau_{\text{eq}} \sim t_w$ holds only for $t_w < 10^3$ (Fig. 1b). Second, the parameter k , from which the aging length ξ_{ag} is derived, is extracted from the data with $t_w < 10^3$ (see Fig. 5b). In Fig. S17c-d, we use arrows to indicate the time at which the logarithmic decay, $F_w(t_w) \sim -k \ln t_w$, ends.

It can be seen that the growth of S_0 emerges after this logarithmic regime. We can therefore safely conclude that crystallization and phase separation are negligible within the aging dynamics under investigation.

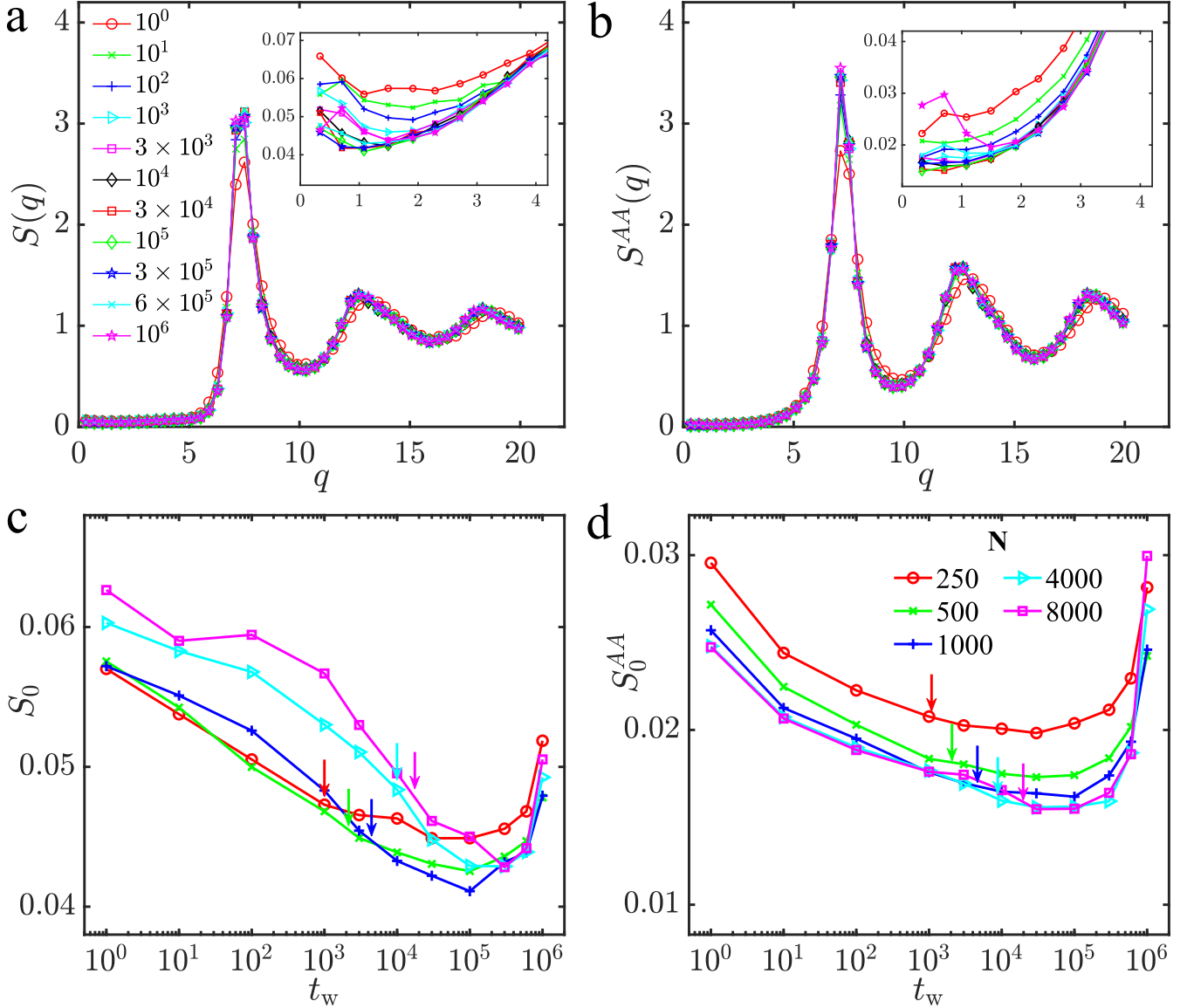


FIG. S17. Static structural factor $S(q)$ for the WCA model. Data are obtained at $T = 0.25$, quenched from $T_{\text{eq}} = 5$. The structure factor for (a) all particles and (b) large particles, at a few different t_w . Inset is the close-up for small q . Estimates for S_0 and S_0^{AA} are obtained by taking the mean of the five data points corresponding to the smallest q . (c) S_0 and (d) S_0^{AA} as functions of t_w , for a few different N . The arrows indicate the end of the logarithmic decay of $F_w(t_w)$.

C. Estimate of the onset temperature for amorphous silica

The onset temperature T_{onset} is defined as the characteristic temperature below which glassy dynamics appear. For amorphous silica, T_{onset} has not yet been reported in the literature. In this study two independent methods are employed to estimate T_{onset} . The first method is based on the T -dependent behavior of the α -relaxation time $\tau_{\text{eq}}(T)$ in supercooled liquids. One defines T_{onset} at the point where $\tau_{\text{eq}}(T)$ departs from the high- T Arrhenius behavior, $\tau_{\text{eq}}(T) \sim \exp(E_{\infty}/T)$. Applying this criterion to our simulation data gives $T_{\text{onset}} \approx 5800$ K (see Fig. S18a). Note that for amorphous silica, $\tau_{\text{eq}}(T)$ is also Arrhenius at low T (with a constant, but larger activation energy than E_{∞}), consistent with the well-known fact that amorphous silica forms strong glasses.

The second method is based on the T -dependent behavior of the potential energy $E_{\text{IS}}(T)$ of inherent structures [92]. The inherent structures at zero temperature are obtained by minimizing the energy of configurations initially equilibrated at T using the FIRE algorithm [93]. The high- T and low- T data of $E_{\text{IS}}(T)$ are fitted by two linear functions, whose intersection defines $T_{\text{onset}} \approx 5800$ K (see Fig. S18b). The above two methods give a consistent T_{onset} within the numerical uncertainty.

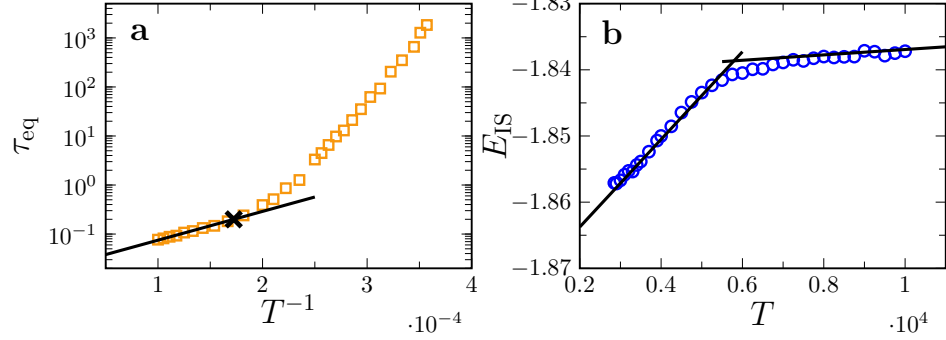


FIG. S18. Onset temperature T_{onset} in the amorphous silica model. (a) α -relaxation time τ_{eq} as a function of $1/T$. The high- T data are fitted to the Arrhenius law (line), and the departing point indicates T_{onset} . (b) Inherent structure energy E_{IS} as a function of T . The two lines represent linear fitting to low- T and high- T data, whose intersection defines T_{onset} . Data are obtained for $N = 1536$.

D. Nonergodicity order parameter

The nonergodicity parameter f is defined by $f = \lim_{t \rightarrow \infty} F_{\text{eq}}(t)$, where $F_{\text{eq}}(t)$ is the equilibrium incoherent scattering function. For the aging data, f corresponds to the plateau value of $F(t_w, t_w + t)$ by sending $t_w \rightarrow \infty$ first (equilibrium limit) and then $t \rightarrow \infty$ (large-time limit); see Fig. 1c. Figure S19 shows the data of f obtained for both WCA and amorphous silica models. Interestingly, the data nearly collapse if plotted as functions of the rescaled temperature T/T_{WEB} .

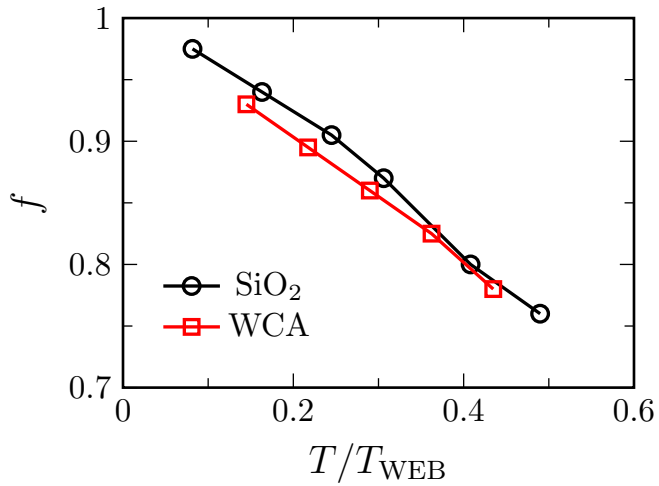


FIG. S19. Nonergodicity parameter f with respect to the rescaled temperature T/T_{WEB} , for WCA and amorphous silica models.

E. Exponent β

According to our theory, the aging function follows logarithmic behavior in the intermediate-time regime, $F_w(t_w) \sim -k \ln t_w$. For mean-field models (e.g., REMs), $k \sim 1/N$ (see Eq. 5). For finite-dimensional models, such as the WCA and amorphous silica models, we find that $k \sim N^{-\beta}$ as shown in Fig. 5(c, f) (in the WCA model, k becomes a constant when $N > n$). The T -dependent exponent β is reported in Fig. S20. For both models, $\beta \approx 0.1 - 0.4$, which is considerably smaller than the mean-field value $\beta = 1$. It is unclear if this discrepancy comes from finite-dimensional effects or pre-asymptotic effects due to insufficiently large systems.

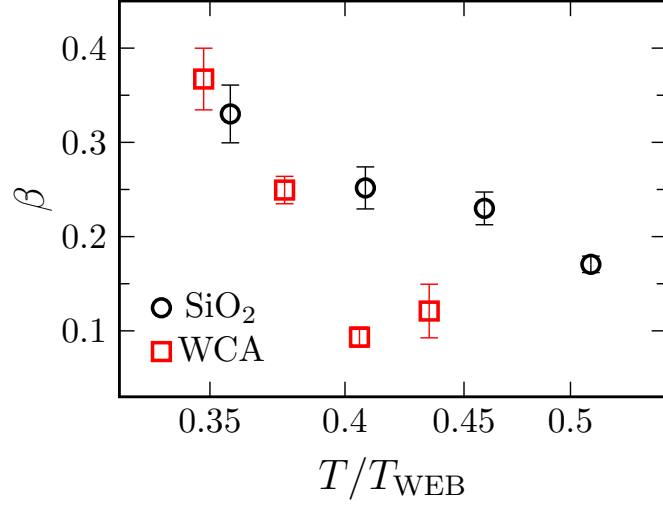


FIG. S20. Exponent β as a function of $\hat{x} = T/T_{\text{WEB}}$ in WCA and amorphous silica models.